Formation of a Quasi-Universal Internal Wave Spectrum by Wind Forcing Alone: Idealized Modeling and Mooring Observations

Qian Zhang,[a,b] Zhiwu Chen,[a] Zhiyu Liu,[c] Lixin Qu,[d] Huaihao Lu,[d] Yuhan Sun,[a,b] Qingyou He,[a,e] Jiexin Xu,[a] Yankun Gong,[a] AND Shuqun Cai[a]

[a] *State Key Laboratory of Tropical Oceanography, South China Sea Institute of Oceanology, Chinese Academy of Sciences, Guangzhou, China*

[b] *University of Chinese Academy of Sciences, Beijing, China*

[c] *State Key Laboratory of Marine Environmental Science, and Department of Physical Oceanography, College of Ocean and Earth Sciences, Xiamen University, Xiamen, China*

[d] *School of Oceanography, Shanghai Jiao Tong University, Shanghai, China*

[e] *Guangdong Key Lab of Ocean Remote Sensing, South China Sea Institute of Oceanology, Chinese Academy of Sciences, Guangzhou, China*

Corresponding author: Zhiwu Chen, zhiwuchen@scsio.ac.cn

Early Online Release: This preliminary version has been accepted for publication in *Journal of Physical Oceanography*, may be fully cited, and has been assigned DOI 10.1175/JPO-D-25-0199.1. The final typeset copyedited article will replace the EOR at the above DOI when it is published.

ABSTRACT

Oceanic internal waves (IWs) play a key role in diapycnal mixing that sustains the global overturning circulation. Their energy follows a quasi-universal Garrett-Munk (GM) spectrum, traditionally attributed to nonlinear wave-wave interactions under combined wind and tidal forcing. However, growing evidence points to the importance of eddy-wave interactions, but the specific energy contributions from mesoscale and submesoscale motions to this GM spectrum remain unclear. More importantly, the generation of this GM spectrum by eddy-wave interactions has not been observed in the real ocean. In the present work, an idealized numerical model is used to simulate the formation of a GM-like spectrum by eddy-wave interaction under wind forcing alone. Energy transfers are diagnosed in both Eulerian and Lagrangian coordinates using a multi-scale energy and vorticity analysis. It is found that IW energy supplied by mesoscale eddies is comparable to that from submesoscale motions in Lagrangian coordinate, whereas this mesoscale contribution appears much weaker in Eulerian coordinate. Vertically, mesoscale eddies transfer energy to IWs in the upper ocean, while this energy transfer is reversed in the pycnocline. In-situ mooring observations from the Southern Ocean further support the role of eddies in facilitating the generation of a GM-like spectrum under wind forcing alone. Together, these findings clarify the energy pathways through which mesoscale and submesoscale dynamics energize IWs and offer new insight into the dynamical processes that help maintain the GM spectrum.

SIGNIFICANCE STATEMENT

A quasi-universal internal wave (IW) spectrum is traditionally thought to be created by wave-wave interactions through simultaneous wind and tidal forcing. Using idealized simulations and Southern Ocean observations, this study provides evidence that wind forcing over an eddying ocean can generate a GM-like spectrum. Lagrangian energy transfer analyses reveal comparable mesoscale and submesoscale contributions to IW energy, whereas direct extraction of mesoscale energy is less apparent in Eulerian coordinate. Vertically, mesoscale eddies energize IWs in the upper ocean, while IWs return energy to mesoscale eddies in the pycnocline, thus limiting the penetration of wind-induced IWs. These results clarify the dynamical pathways feeding IWs, providing new insights into the formation of a GM-like spectrum under wind forcing alone.

Accepted for publication in *Journal of Physical Oceanography*. DOI 10.1175/JPO-D-25-0199.1

1. Introduction

Oceanic internal waves (IWs) have attracted extensive attentions over the years due to their critical roles in turbulent mixing, the global meridional overturning circulation, and the climate system (Ferrari & Wunsch 2009; Whalen et al. 2020). Near-inertial waves (NIWs) are the lowest-frequency IWs and usually occupy the most IW energy. They are primarily generated by time-varying winds (Fu 1981; Gill 1984) but can also arise from geostrophic adjustment of balanced motions and other processes (Nagai et al. 2015). They are widely distributed throughout the global ocean and usually exhibit strong vertical shear, and are thus recognized as a key driver of ocean energy cascade and mixing processes (Munk 1981; Alford et al. 2016).

Observations reveal that IW energy in the open ocean is continuously distributed in frequency-wavenumber space and exhibits a quasi-universal spectral structure. In a log-log coordinate, the IW energy spectrum exhibits a spectral slope close to -2 in both high-frequency and high-wavenumber ranges, which is well described by the Garrett-Munk (GM) IW spectrum (Garrett & Munk 1972; 1975; 1979). This empirical spectrum not only matches key observational characteristics but also has been shown to be close to a stationary solution of the kinetic equation (Polzin & Lvov 2011). As such, the GM spectrum is regarded as the most important conceptual development of IWs in the last 100 years (Wunsch & Ferrari 2018).

The underlying mechanism for the generation of the GM spectrum is commonly attributed to nonlinear interactions among IWs. The classical paradigm is that winds produce NIWs, barotropic tidal flows over topography create internal tides, and then nonlinear wave-wave interactions fill out the IW continuum (e.g., Müller et al. 1986; Arbic et al. 2018). These interactions among IWs transfer energy across different frequencies and wavenumbers, effectively driving an energy cascade of NIWs and internal tides and thereby giving rise to the quasi-universal GM spectrum (McComas & Bretherton 1977; Lvov et al. 2012; Olbers et al. 2012). Realistic global ocean models with both wind and tidal forcing have shown that a partial IW continuum exists in these models (Müller et al. 2015; Rocha et al. 2016). Using an idealized model, Sugiyama et al. (2009) showed that a GM-like IW spectrum can be created and maintained only when energy is supplied from both wind and tidal forcing. In their setup, however, IWs were not explicitly modeled; the system was initialized with idealized, low-mode NIWs and/or semidiurnal internal tides in a flat-bottomed ocean. In contrast, Chen et al. (2019) used an idealized model that explicitly includes tidal forcing over steep topography, and showed that tidal forcing alone can generate a GM-like IW spectrum. In their mechanism,

Accepted for publication in *Journal of Physical Oceanography*. DOI 10.1175/JPO-D-25-0199.1

strong tidal flow over rough topography generates large amplitude internal tides, which break and generate NIWs by triadic resonant interaction. Further wave-wave interactions subsequently generate a GM-like IW spectrum. This finding might explain why a universal IW spectrum exists in the deep ocean where the effect of wind forcing is virtually absent. However, this mechanism still falls within the nonlinear wave-wave interaction regime.

Mesoscale eddies are the primary carriers of low-frequency kinetic energy (KE) in the world oceans. In recent years, an increasing number of simulation studies points to the crucial role of eddy-wave interactions in driving forward energy cascade of mesoscale eddies and redistributing IW energy across different spatiotemporal scales (Barkan et al. 2017; 2021; Delpech et al. 2024; Shaham & Barkan 2025). Mesoscale eddies play a multifaceted role in modulating IW dynamics through processes such as advection, refraction, and modulation by background vorticity (Kunze 1985; Polzin 2010; Thomas et al. 2024). These processes alter the spatial coherence, wavelength, and effective frequency of NIWs. Beyond these well-known effects, recent studies have increasingly highlighted additional mechanisms. For example, mesoscale eddies can act as catalysts that scatter IW energy across scales via induced diffusion (Kafiabad et al. 2019; Savva et al. 2021; Cox et al. 2023; Dong et al. 2023), serve as direct energy sources that inject energy into IWs (Taylor & Straub 2020; Barkan et al. 2021), and modulate the spectral energy distribution through nonlinear interactions (Thomas 2023; Skitka et al. 2024; Shaham & Barkan 2025). As to the formation of an IW continuum spectrum, Barkan et al. (2017) used an idealized numerical model and analyzed IW-induced eddy energy cascade, showing that wind forcing alone can generate a GM-like IW spectrum. Yang et al. (2023) used a realistic North Atlantic simulation, also by wind forcing alone, and demonstrated that mesoscale eddies facilitate the rapid formation of an IW continuum. More recent simulations of the Iceland Basin and California Current (Barkan et al. 2024; Delpech et al. 2024) offered detailed diagnostics of eddy-wave energy transfers, but formation of a GM-like spectrum was not the focus of these studies. Together, these studies have implied that eddy-wave interactions could generate a GM-like IW spectrum, which is complementary to the traditional paradigm of wave-wave interactions.

However, the previous eddy-wave simulations primarily focused on how IWs facilitate forward energy cascade of mesoscale eddies. The specific energy transfers from mesoscale and submesoscale motions to the GM-like IW continuum still remain unclear. In the present study, we study these energy transfers by applying a diagnostic framework (the MS-EVA approach, see Section 2c) that has not been utilized by the previous mentioned studies. Energy transfers

Accepted for publication in *Journal of Physical Oceanography*. DOI 10.1175/JPO-D-25-0199.1

in Eulerian versus Lagrangian perspectives are also compared and the underlying physical mechanisms are identified, providing new insight into the formation of a GM-like spectrum. More importantly, generation of this GM-like spectrum by eddy-wave interactions through wind forcing alone has not been observed in the real ocean and the present study fills this gap by using mooring observations from the Southern Ocean. Generally, the wind-forcing-alone effect is difficult to be observed in a real ocean, partly due to the complicated influence of internal tides. The Southern Ocean, characterized by strong wind forcing over intense mesoscale eddies and yet with weak internal tides (e.g., Savage et al. 2017), offers a unique natural place to test whether the interaction between mesoscale eddies and wind-forced NIWs can produce a GM-like spectrum.

The remainder of this paper is organized as follows. Section 2 describes the numerical model and methods used for analysis. Section 3 presents the formation of a GM-like IW spectrum in numerical simulations and in-situ observations, complemented by detailed energy transfer and mechanism analyses. Finally, key conclusions are summarized in Section 4.

2. Data and Methods

a. Numerical modeling

An idealized wind-driven reentrant channel model representing the Antarctic Circumpolar Current is constructed based on the Massachusetts Institute of Technology general circulation model (MITgcm, Marshall et al. 1997). The model domain (Fig. 1a) is rectangular with east-west (x-axis) periodic boundary conditions, and a 100-km-wide sponge layer is applied near each north-south (y-axis) boundary to avoid wave reflections. The model domain is 420 km in the x-axis, 800 km in the y-axis (centered at a latitude of 55° with $f = 1.2 \times 10^{-4}$ rad/s and on a β-plane with $\beta = 1.3 \times 10^{-11}$ $\mathrm{m^{-1}s^{-1}}$), and 2 km in the z-axis. Even though application to the Southern Ocean is considered, a positive f is used without loss of generality. The model horizontal resolution is 2 km and the vertical one is 10 m. We adopt the same viscosity, diffusivity, and vertical mixing settings as in the LLC4320 configuration, including the K-profile parameterization (KPP) scheme for vertical mixing. LLC4320 is a global ocean simulation at a 1/48° horizontal resolution, conducted on the Latitude-Longitude-Cap (LLC) grid using the MITgcm (Rocha et al. 2016). The designation "4320" refers to the number of longitudinal grid points at the equator, corresponding to a horizontal resolution of approximately 2 km. For bottom drag, our model uses a quadratic bottom drag with a drag coefficient of 0.0021 $\mathrm{s^{-1}}$. No surface relaxation is applied to the temperature field. The model

Accepted for publication in *Journal of Physical Oceanography*. DOI 10.1175/JPO-D-25-0199.1

starts from a quiescent state with stratification depending on both depth and latitude (Figs. 1a and 1b), as in Tort and Winters (2018). The central region within y = ±200 km is used for subsequent analyses.

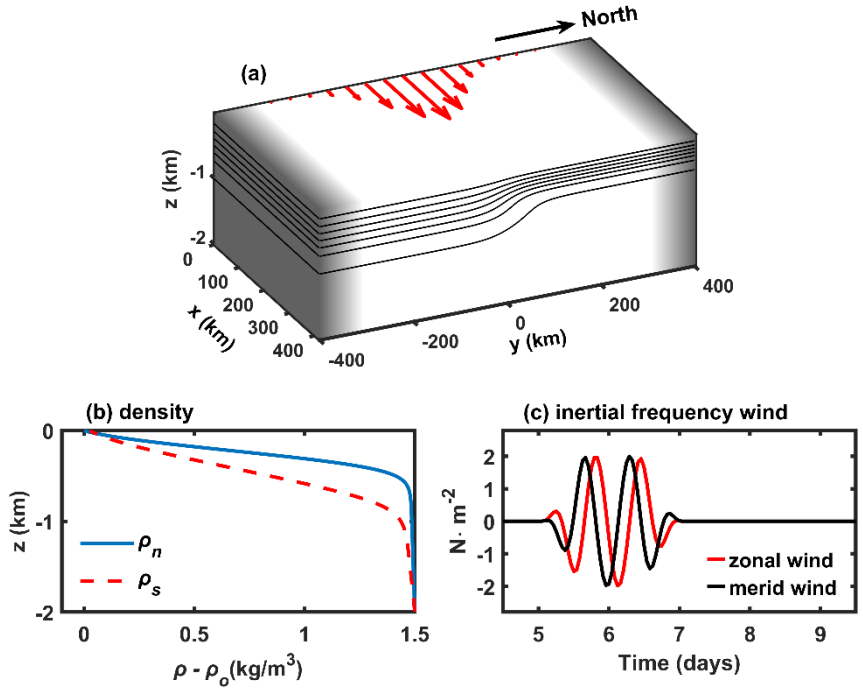

FIG. 1. Model configurations. (a) Schematic diagram of the model setup. Wind forcing (red arrows) is applied in the middle region and is meridionally confined. A 100-km-wide sponge layer is applied near both the northern and southern boundaries (grey shading). Six sloping isopycnals are also overlain. (b) The initial density profiles on the northern (ρ_n) and southern (ρ_s) boundaries in the first stage of the model run. (c) Time series of the forcing wind stress that contains two days of inertial-frequency winds applied in the wave-only and eddy-wave cases.

The model run is divided into two stages. In the first stage, the model is driven by a steady zonal wind for 240 days until eddies have fully developed. The wind stress is $0.2 \cdot \mathrm{sech}^2(y/L_0)$ N/m^2, where $L_0 = 100$ km. The slantwise isopycnals and the horizontally sheared winds jointly facilitate the generation of eddies. After the eddy field is established, the steady wind is turned off in the second stage to prevent nonlinear coupling. This setup, though idealized, allows us to better isolate the effect of a transiting storm on the pre-existing eddy field. It also reflects some oceanic conditions where wind forcing is often intermittent due to seasonal transitions, wind jet shifts, or synoptic variability. Thus, this model setup represents an initial value problem, rather than a forced-dissipative system. In the second stage, three different cases are performed for 27 days. In the eddy-only case, eddies evolve freely without external forcing. In the eddy-wave case, an inertial frequency wind $2 \cdot \mathrm{sech}^2(y/L_0) \cdot \exp(-ift) \cdot W(t)$ N/m^2, where $W(t)$ is a symmetric Tukey window confining the duration of the wind, is exerted for two days (days 5-7 in Fig. 1c) to simulate a transiting storm. Wind-generated NIWs coexist

Accepted for publication in *Journal of Physical Oceanography*. DOI 10.1175/JPO-D-25-0199.1

with mesoscale eddies in this case. To further compare the situations with and without eddies, a third case (wave-only) is performed, which is forced by the same inertial frequency wind but starts from a quiescent state. The initial temperature profile is obtained by horizontally averaging the temperature field at the final moment of the first stage of cases eddy-only and eddy-wave.

b. Spatial energy transfers: the coarse-graining method

To quantify spatial KE transfer associated with eddy-wave interactions, we employ a coarse-graining method (Aluie et al. 2018; Storer et al. 2022), implemented via the FlowSieve package (Storer et al. 2023). This method is general, mathematically exact, and does not rely on assumptions of homogeneity or isotropy, making it particularly well-suited for analyzing multiscale dynamics. It can be applied at any geographic location and at any instant of time, thereby helping elucidate underlying energy pathways in our simulations.

The essence of the method lies in the application of a spatial filter to decompose the flow field into large-scale (scales > ℓ) and fine-scale (scales < ℓ) components, where ℓ is a user-defined filter scale. Mathematically, for any given field $F(x)$, the coarse-grained field $F_\ell(x)$ is obtained through the convolution of F with a normalized kernel G_ℓ : $F_\ell(x) = G_\ell * F(x)$, where $*$ denotes convolution and G_ℓ is chosen as a top-hat filter in this study. The KE evolution equation of the large-scale flow $\bar{u}_\ell$ is as follows:

$$\frac{\partial}{\partial t}\rho_0 \frac{|\overline{\boldsymbol{u}}_\ell|^2}{2} + \nabla \cdot \boldsymbol{J}_\ell^{transport} = -\Pi_\ell - \rho_0 \nu |\nabla \overline{\boldsymbol{u}}_\ell|^2 + \bar{\rho}_\ell g \cdot \overline{\boldsymbol{u}}_\ell + \rho_0 \overline{\boldsymbol{F}}_\ell^{forcing} \cdot \overline{\boldsymbol{u}}_\ell. \qquad (1)$$

In this equation, the terms from left to right represent: (i) temporal evolution of large-scale KE, (ii) spatial transport, (iii) nonlinear energy transfer across scale ℓ, (iv) dissipation caused by molecular viscosity, (v) conversion between available potential energy (APE) and KE, and (vi) energy injection from external forcing. A full derivation of these terms is available in Aluie et al. (2018).

Our analysis focuses on the nonlinear energy transfer term Π_ℓ, which quantifies the KE transfer between large and small scales. It is calculated as $\Pi_\ell(\boldsymbol{x}) = -\rho_0 \overline{\boldsymbol{S}}_\ell : \bar{\boldsymbol{\tau}}_\ell(\boldsymbol{u}, \boldsymbol{u})$, representing that the large-scale strain tensor $\overline{\boldsymbol{S}}_\ell$ acts against subfilter-scale stress $\bar{\boldsymbol{\tau}}_\ell(\boldsymbol{u}, \boldsymbol{u})$. A positive Π_ℓ indicates energy transfer from large to small scales across the specified spatial scale (forward cascade), whereas a negative value indicates upscale energy transfer (inverse cascade). This term contains all the information needed in our subsequent spatial energy transfer analyses. In our implementation, we use horizontal filter scales ranging from 10 to 200 km, with an

Accepted for publication in *Journal of Physical Oceanography*. DOI 10.1175/JPO-D-25-0199.1

increment of 10 km. The resulting scale-dependent energy transfers support a systematic investigation of multiscale dynamics.

c. Temporal energy transfers: MS-EVA

To further explore temporal energy transfers, the Multi-Scale Energy and Vorticity Analysis (MS-EVA) is used. MS-EVA is developed to investigate multiscale dynamical interactions in geophysical fluids that are intermittent in space and time (Liang 2016). It is based on a wavelet-based functional analysis tool, which is local, orthonormal, and windowed on time scales.

Using the method, the flow is divided into three timescale windows, allowing the KE change in each window to be diagnosed. For example, KE change within window [2] is determined by

$$\frac{\partial}{\partial t}K^{[2]} = \Gamma_K^{[0]\to[2]} + \Gamma_K^{[1]\to[2]} + \Gamma_K^{[0]\oplus[1]\to[2]} - b^{[2]} - \nabla\cdot Q_K^{[2]} - \nabla\cdot Q_P^{[2]} + F_K^{[2]}, \qquad (2)$$

where superscripts enclosed in square brackets indicate timescale windows, subscript K represents KE and P represents pressure work. MS-EVA divides the energy fluxes into four types: (i) energy transfers among different timescale motions (term Γ); (ii) buoyancy conversions (term b), denoting conversions between KE and APE; (iii) energy transports across spatial locations (term Q); (iv) external work or energy dissipations (term F).

In the present study, the inertial period is 14.5 hours, and two timescale cutoffs are set at 6.7 days and 20.2 hours (corresponding to a frequency of 0.7f). Thus, window [0] refers to mesoscale eddies, window [2] refers to IWs, and window [1] refers to the intermediate frequency band (mostly submesoscale motions). Thus, the term $\Gamma_K^{0\to2}$ (denoted as TK02 later) represents energy transfer from window [0] to window [2], i.e., energy transfer from mesoscale eddies to IWs. The term $\Gamma_K^{1\to2}$ (denoted as TK12 later) represents energy transfer from submesoscale motions to IWs. The term $\Gamma_K^{0\oplus1\to2}$ (denoted as TK012 later) represents energy transfer from the interaction between mesoscale and submesoscale motions to IWs. These terms facilitate our exploration of detailed temporal energy transfers underlying the physical phenomena.

d. Lagrangian transformation and filtering

Lagrangian transformation is used to get flow information on Lagrangian particles, and Lagrangian filtering is used to obtain the IW field. Lagrangian filtering uses the more sophisticated definition of an IW as "a high-frequency motion as measured moving with the

Accepted for publication in *Journal of Physical Oceanography*. DOI 10.1175/JPO-D-25-0199.1

flow", thus filtered flows would contain only IWs (Shakespeare et al. 2021). For a given time slice, the approach seeds initial particles at every model grid point, performs forward and backward advection, and then performs the final filtering on the Lagrangian-transformed data. For the Lagrangian frequency spectrum and MS-EVA analyses, Lagrangian-transformed velocities are constructed by advecting particles forward and backward in time using a window of 13.5 days (half of the 27 days for analyses). For Lagrangian filtering, particle advections are executed within a moving window of 6 days as in Yang et al. (2023). Then, IWs are obtained by high-pass filtering with a cutoff frequency of 0.7f.

3. Results and discussion

a. Flow fields in the simulations

The analysis begins with an examination of the flow field characteristics. In the second stage of the simulations, the steady wind forcing is turned off, and at day 5, a two-day inertial wind forcing is imposed to simulate the passage of a storm. To investigate the dynamical adjustment of the flow field during the second stage, we analyze the evolution of KE and APE anomalies integrated over the upper 1000 m (Fig. 2). KE is computed as the volume integral of $\frac{1}{2} \cdot \rho \cdot (u^2 + v^2 + w^2)$, and APE as the integral of $\frac{g^2 \rho'^2}{2\rho_0 N^2}$ (Winters et al., 1995; Kang & Fringer, 2010), where ρ' is defined as density perturbation from the horizontal average, g = 9.81 m/s^2 is the gravitational acceleration, ρ_0 = 1025 kg/m^3 is a reference density, and $N^2 = \left(-\frac{g}{\rho_0}\right)\frac{\partial \rho}{\partial z}$ is the horizontally averaged stratification.

In the eddy-only case (black lines), both KE and APE anomalies exhibit a gradual decline over time, reflecting the natural dissipation of mesoscale eddies in the absence of external forcing. The situation of the eddy-wave case (red lines) follows the same evolution as the eddy-only case during the first 5 days. At day 5, a transient inertial wind forcing is introduced, resulting in a rapid increase in both KE and APE. To isolate the storm influence, we plot the difference between the eddy-wave and eddy-only cases (cyan lines), representing the net effect of the storm over an eddying ocean. This allows direct comparison with the wave-only case (blue lines), which reflects storm forcing over a quiescent ocean. For KE, the storm-induced anomaly in the presence of eddies is overall smaller than the wave-only case, likely reflecting enhanced dissipation. The storm-induced APE anomaly is also overall reduced relative to the wave-only case. These nonlinear modulations highlight the importance of the eddy field during storm passage and show that storm-driven IWs cannot be fully understood without considering their interactions with the background eddy field.

Accepted for publication in *Journal of Physical Oceanography*. DOI 10.1175/JPO-D-25-0199.1

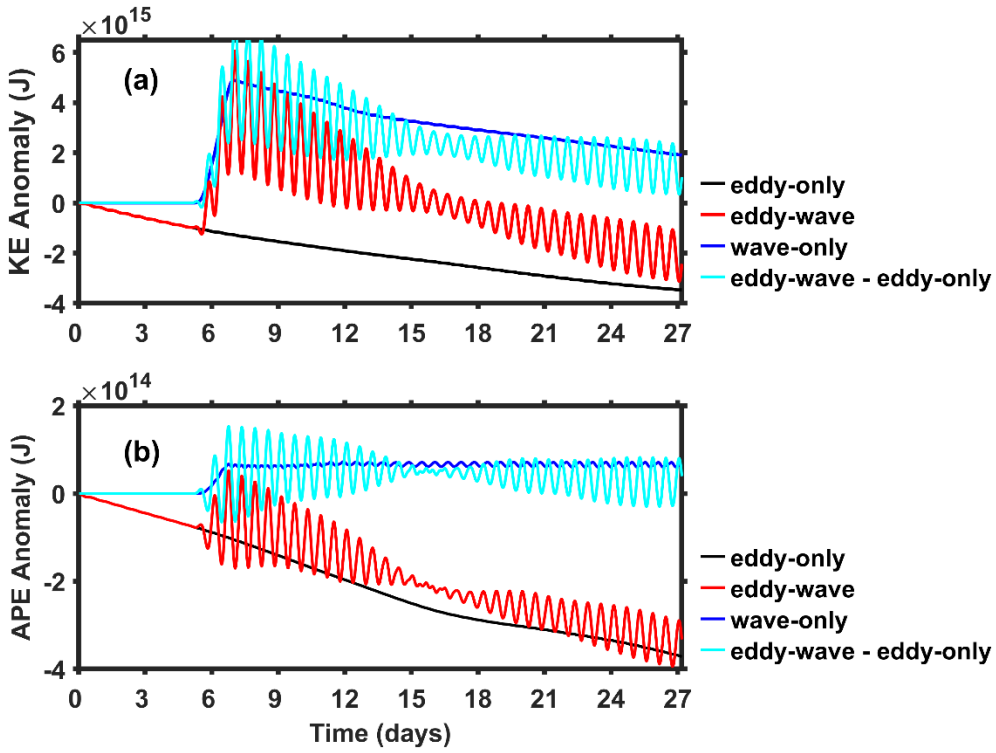

FIG. 2. Time evolution of volume-integrated (a) kinetic and (b) available potential energy anomalies for cases eddy-only (black), wave-only (blue), and eddy-wave (red) during the second stage of the simulations. The difference between eddy-wave and eddy-only cases (cyan) is also plotted as a reference. Energy anomalies are computed as the deviation of instantaneous energy values from their respective initial values at the beginning of the second stage.

Flow fields represented by the Rossby number at day 27 in the second stage of simulations are shown in Fig. 3. Time-averaged vertical stratification profiles are shown on the left-hand side of each panel, with the mixed layer depth (MLD) indicated by horizontal dashed lines. The MLD is defined as the depth where the temperature decreases by 0.2°C relative to the surface temperature. Mean MLD values are 65 m for the eddy-only case, 81 m for the wave-only case, and 80 m for the eddy-wave case. In the wave-only case (Fig. 3a), NIWs are effectively generated by the inertial frequency wind forcing and banded wave structures develop in the flow field. In the eddy-only case (Fig. 3b), the flow field is characterized by abundant mesoscale eddies. Submesoscale eddies, fronts, and filaments are also present in the flow field. In the eddy-wave case (Fig. 3c), NIWs and mesoscale eddies are simultaneously present. They interact with each other, introducing finer-scale structures into the flow field. These small-scale features appear as oscillatory wave patterns superimposed on the larger mesoscale eddies, leading to an overall increase in flow complexity. Compared to the eddy-only case, the eddy-wave case exhibits enhanced small-scale wave activity, manifesting as high-frequency velocity fluctuations and increased vorticity gradients.

Accepted for publication in *Journal of Physical Oceanography*. DOI 10.1175/JPO-D-25-0199.1

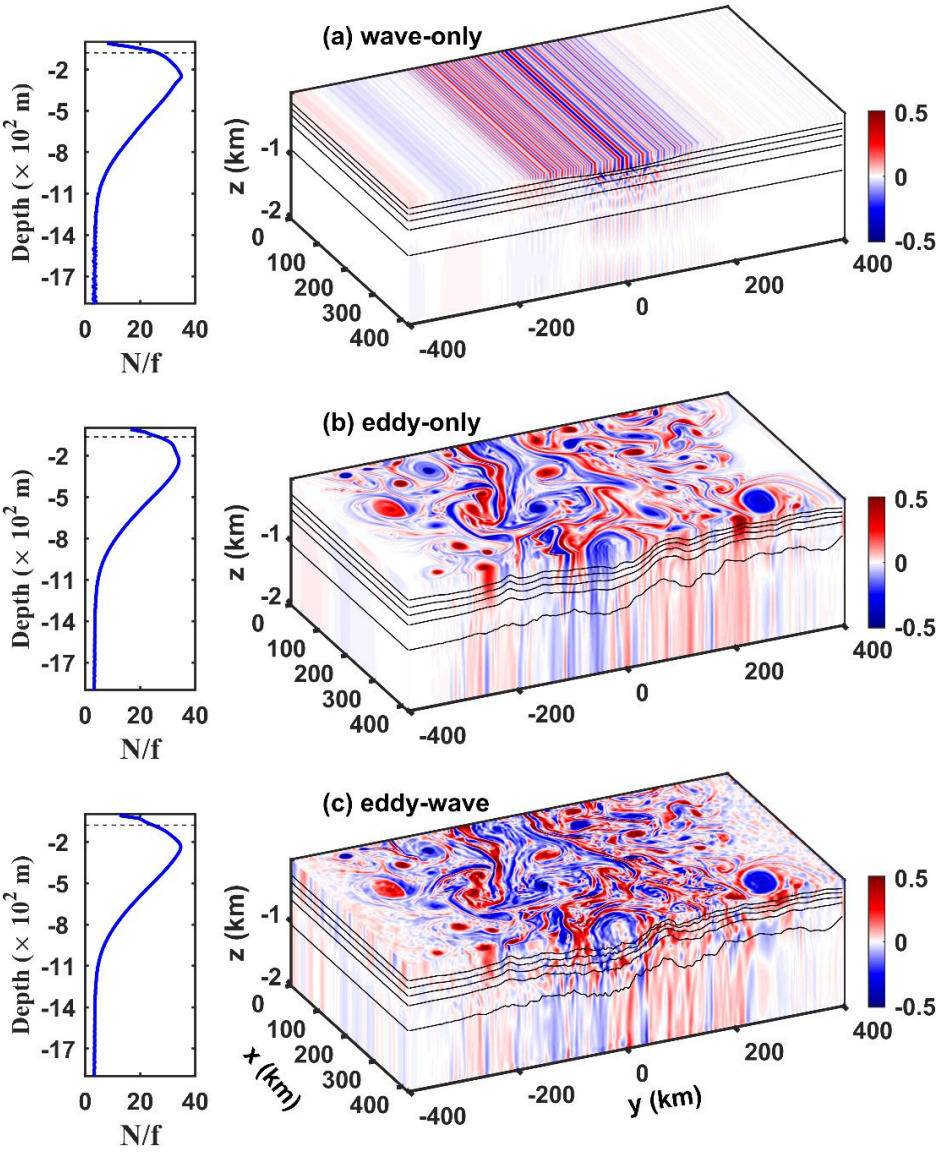

FIG. 3. Snapshots of Rossby number (vertical relative vorticity normalized by the local Coriolis frequency) of (a) the wave-only case, (b) the eddy-only case, and (c) the eddy-wave case at day 27 in the second stage of simulations. Five density contours with an interval of 0.15 kg · m^{-3}are overlain. Vertical stratification profile, averaged in time and horizontally, is shown on the left-hand side of each panel, with the mixed layer depth indicated by a horizontal dashed line.

The depth and time distributions of near-inertial kinetic energy (NIKE) and super-inertial kinetic energy (SIKE) for wave-only and eddy-wave cases are presented in Fig. 4. Here, NIKE is obtained via band-pass filtering within the frequency range of 0.85*f*-1.15*f*, while SIKE is extracted through high-pass filtering with a cutoff frequency of 1.5*f*. The applied inertial-frequency wind forcing leads to an efficient injection of energy into inertial oscillations, resulting in a pronounced enhancement of NIKE. In the wave-only case, NIKE is predominantly confined to the upper 200 m (Figs. 4a-4b). Notably, there is minimal energy penetration into the ocean interior, indicating that in the absence of mesoscale eddies, NIWs are largely trapped near the surface. In contrast, the eddy-wave case (Fig. 4c) reveals a

Accepted for publication in *Journal of Physical Oceanography*. DOI 10.1175/JPO-D-25-0199.1

markedly different NIKE distribution. Within several days after the initial wind forcing, NIKE propagates to deeper depths, facilitated by the presence of mesoscale eddies. This result underscores the role of eddies in modulating the vertical energy flux of NIWs, effectively extending the influence of mesoscale eddies into deeper layers.

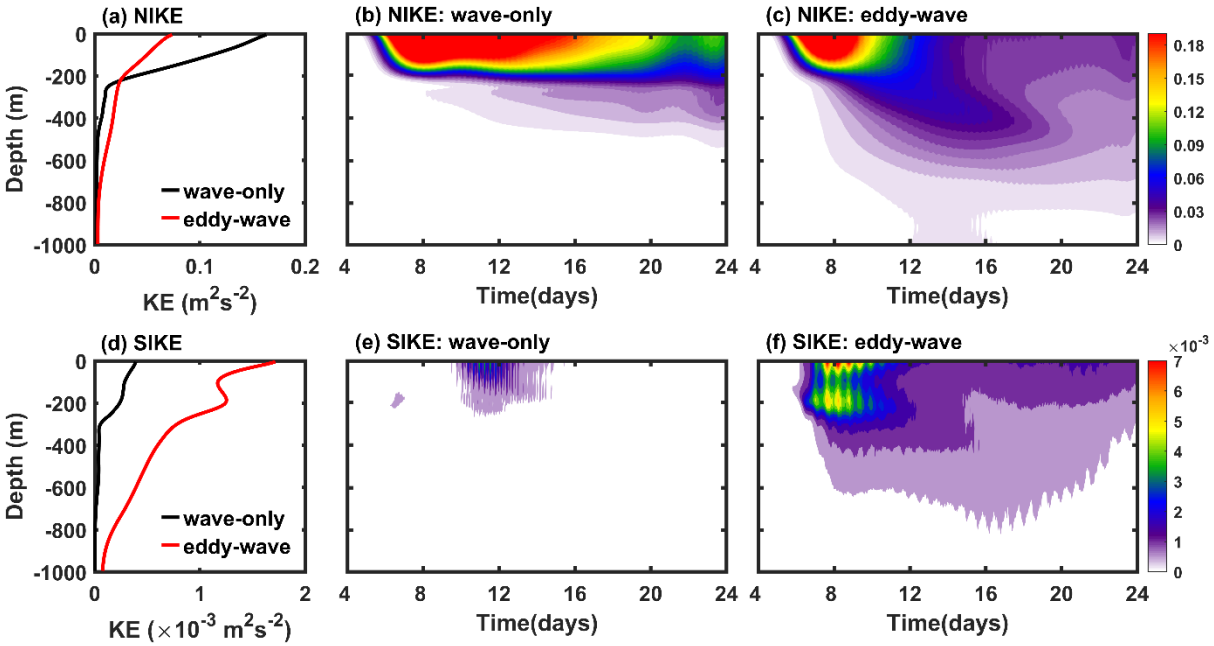

FIG. 4. Distributions of IW energy in wave-only and eddy-wave cases during the second stage of simulations. (a) Vertical distribution of horizontally-averaged and time-mean near-inertial kinetic energy (NIKE). (b) Depth-time distribution of NIKE in the wave-only case. (c) The same as (b) but for the eddy-wave case. (d)-(f) are the same as those in (a)-(c), but for super-inertial kinetic energy (SIKE).

Furthermore, SIKE remains weak in the wave-only case (Figs. 4d-4e), indicating that in the absence of eddies, there is limited generation of high-frequency IWs. In contrast, in the eddy-wave case, SIKE exhibits a substantial increase (Fig. 4f), with two distinct energy peaks emerging: one within the mixed layer and the other in the pycnocline. This suggests that the interaction between mesoscale eddies and NIWs plays a crucial role in enhancing the generation of high-frequency IWs. In other words, the simultaneous presence of mesoscale eddies and NIWs significantly amplifies the generation of high-frequency IWs, potentially contributing to enhanced turbulent mixing and energy dissipation in the ocean interior.

b. Formation of a GM-like spectrum in the simulations

Simulated frequency and wavenumber spectra are shown in Fig. 5 to assess the impact of mesoscale eddies on IW energy redistributions across spatiotemporal scales. For the eddy-only case, KE mainly resides at the low-frequency end of the spectrum, and the IW energy is weak and decreases dramatically with increasing frequency (red line in Fig. 5a). For the wave-only

Accepted for publication in *Journal of Physical Oceanography*. DOI 10.1175/JPO-D-25-0199.1

case (blue line in Fig. 5a), the spectrum shows several peaks at the inertial frequency and its higher harmonics, indicating that wind-generated NIWs mainly transfer energy to their higher harmonic waves (Niwa & Hibiya 1997). With the simultaneous presence of eddies and NIWs in the eddy-wave case (black line in Fig. 5a), the spectrum develops a slope close to -2 of the GM spectrum. To exclude contributions of horizontal Doppler shifting by sub-inertial fronts and eddies, the frequency spectrum on Lagrangian particles is computed (dotted line in Fig. 5a). The main distinction between the Eulerian and Lagrangian spectra lies in the submesoscale frequency band, since submesoscale motions are entrained by low-frequency flows in the Eulerian coordinate, while little difference exists in the IW band, indicating that Doppler shifting plays a minor role there.

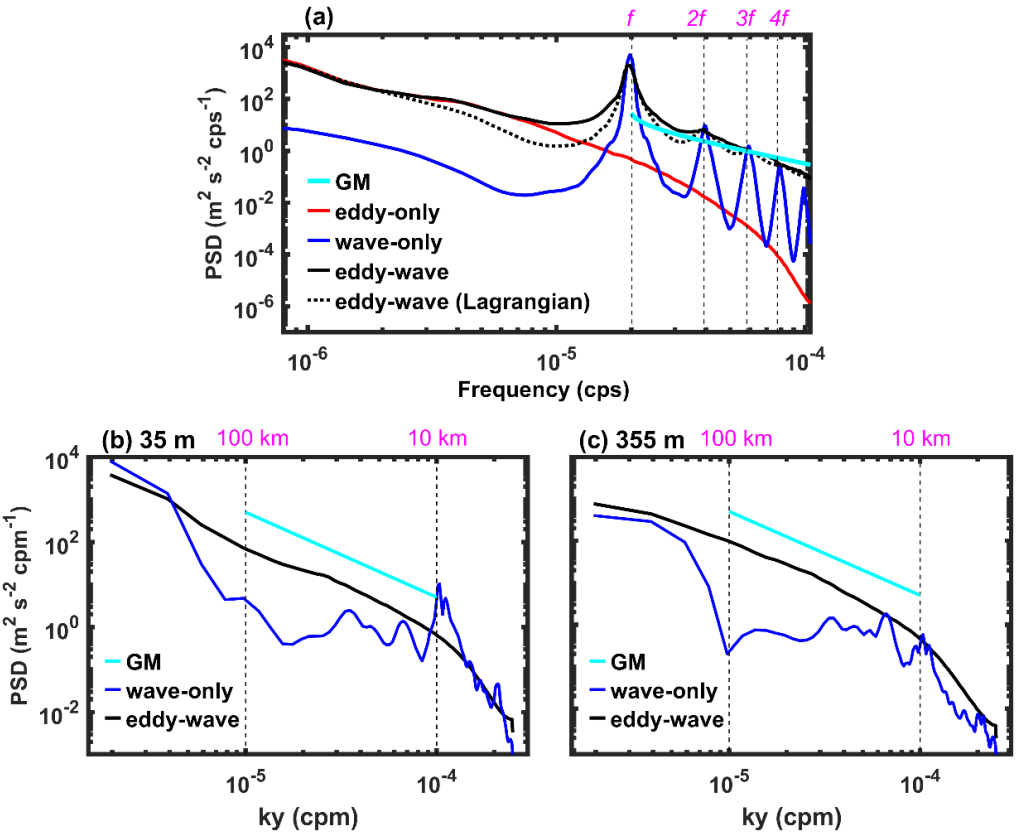

FIG. 5. Kinetic energy distributions in the frequency and wavenumber domain. (a) Domain-averaged frequency spectra of the three cases. The average result of 20-layer spectra (collected every 100 m in depth) is approximated as the domain average. Lagrangian spectrum of the eddy-wave case and the GM spectrum are also plotted for comparison. (b) Wavenumber spectrum of IW energy after Lagrangian filtering at depth 35 m. (c) The same as (b) but at depth 355 m.

The wavenumber spectra of IW energy after Lagrangian filtering for cases wave-only and eddy-wave at two representative depths are presented in Figs. 5(b-c). A key feature is that the presence of mesoscale eddies leads to a significant enhancement of IW energy in the intermediate wavenumber range. This suggests that mesoscale eddies actively redistribute

Accepted for publication in *Journal of Physical Oceanography*. DOI 10.1175/JPO-D-25-0199.1

energy across different spatial scales, modifying the spectral characteristics of IWs. Notably, in the eddy-wave case, the spectral slope becomes substantially closer to the -2 GM spectral slope, which characterizes the observed energy distribution of the IW continuum in the open ocean. The formation of this GM-like spectrum implies that mesoscale eddies play a fundamental role in shaping the IW spectrum, promoting the emergence of a more realistic IW spectral structure.

The frequency-wavenumber spectra are presented in Fig. 6. These spectra reveal that, in the wave-only case, IW energy is primarily concentrated at the inertial frequency and its higher harmonics. In the eddy-wave case, the presence of mesoscale eddies facilitates a more efficient energy redistribution, allowing IW energy to spread across a broad range of spatiotemporal scales. This indicates that mesoscale eddies facilitate spectral broadening, enabling the formation of an IW continuum rather than an energy spectrum dominated by a few distinct peaks. Using realistic numerical simulations in the North Atlantic, Yang et al. (2023) also showed that mesoscale eddies induce a rapid formation of an IW continuum. Thus, both idealized and realistic simulations demonstrate the robustness of the eddy-wave interaction mechanism in shaping structures of the IW continuum.

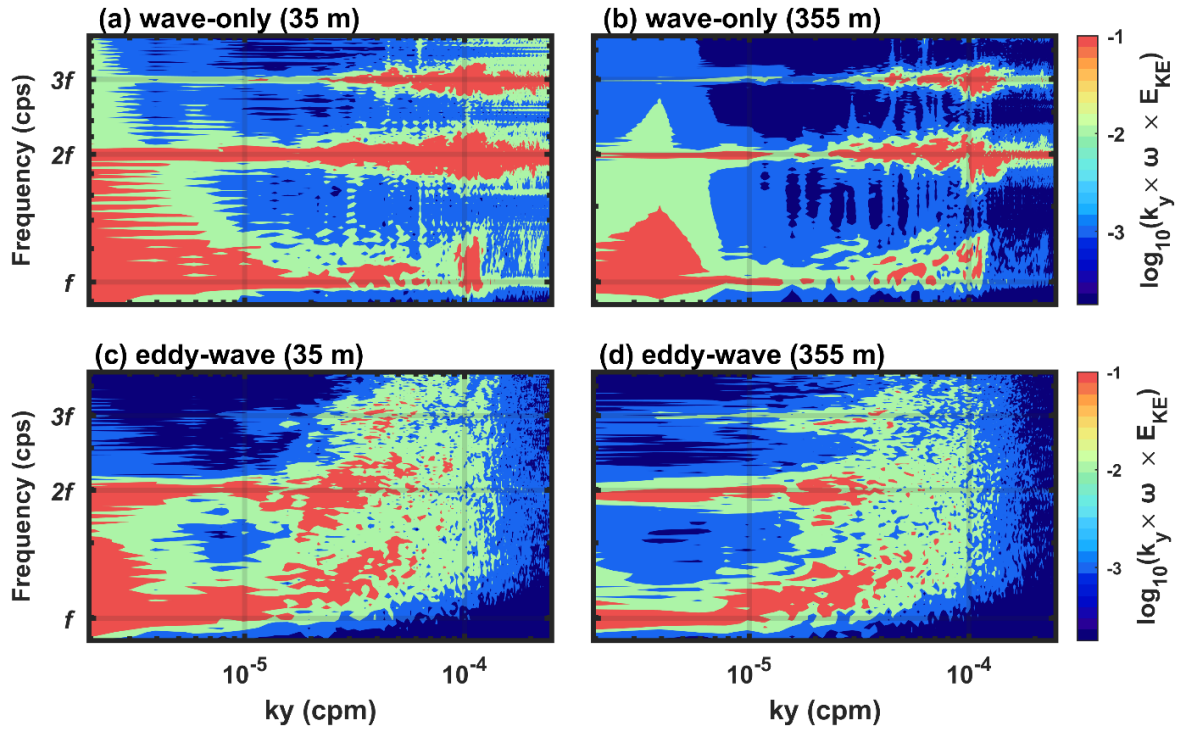

FIG. 6. Frequency-wavenumber spectrum of IW kinetic energy after Lagrangian filtering at depth 35 m for (a) the wave-only case and (c) the eddy-wave case. (b) and (d) are respectively the same as (a) and (c) but at a depth of 355 m.

Accepted for publication in *Journal of Physical Oceanography*. DOI 10.1175/JPO-D-25-0199.1

Considering that mesoscale eddies and submesoscale motions are ubiquitous in the upper ocean, it is clear that high-frequency winds blowing over the upper ocean can easily generate a GM-like spectrum, due to the interaction between mesoscale eddies and wind-generated NIWs. Overall, wind forcing over an eddying ocean can generate a GM-like spectrum, and this is complementary to the situation that tidal forcing alone can generate a GM-like spectrum, as is studied by Chen et al. (2019). Interestingly, these are contrary to the study of Sugiyama et al. (2009), where it was concluded that either wind or tidal forcing alone is not sufficient to generate a GM-like spectrum. It should be noted that Sugiyama et al. (2009) utilized an idealized model that assumed the lowest-mode near-inertial and/or semidiurnal IWs without topography, so that the IW generation forced by winds and/or tides was not explicitly taken into account. However, several studies mentioned in the Introduction (e.g., Barkan et al., 2017; Chen et al., 2019; Yang et al., 2023) and also the present study model the IW generation processes explicitly, either by tide-topography interaction or wind forcing over an eddying ocean, so that multiscale wave-wave or eddy-wave interactions contribute to the generation of a GM-like spectrum.

c. Energy injection by mesoscale and submesoscale processes

Spatiotemporal energy transfers are analyzed to elucidate the role of mesoscale and submesoscale processes in modulating IWs. Spatial energy transfers across a specific length scale are computed by specifying length scales ranging from 10 to 200 km in 10 km increments using the coarse-graining method (Fig. 7). A positive value denotes forward (i.e., from large- to small-scale) energy transfer across the specific length scale, while a negative value denotes the reverse transfer. For the eddy-only case, the energy transfer is always negative across the range of length scales studied, which is consistent with the backward energy cascade of geostrophic turbulence (e.g., Charney, 1971; Müller et al., 2005). With the presence of IWs in the eddy-wave case, forward energy cascade is significantly enhanced (black solid line). The total energy transfer switches from negative to positive at 30 km, indicating a sign change near the Rossby deformation radius of 36 km in the model.

To further diagnose whether the energy source contributing to enhanced forward energy cascade stems from eddies or wind-induced large-scale NIWs, Lagrangian filtering is applied to isolate the IW field, and the corresponding spatial energy transfer is shown in Fig. 7 (black dotted line). The transfer associated with the wave field alone is nearly zero, with only a slight increase at the smallest scales examined. This indicates that wave-wave interactions make only a minor contribution to the observed forward flux. Therefore, the enhanced forward energy

Accepted for publication in *Journal of Physical Oceanography*. DOI 10.1175/JPO-D-25-0199.1

cascade in the eddy-wave case is mainly driven by energy transfer between mesoscale eddies and IWs, rather than by the wave field itself. Combined with the eddy-only case (the red line), these results confirm that eddy-wave interactions are the primary driver of the enhanced forward energy transfer.

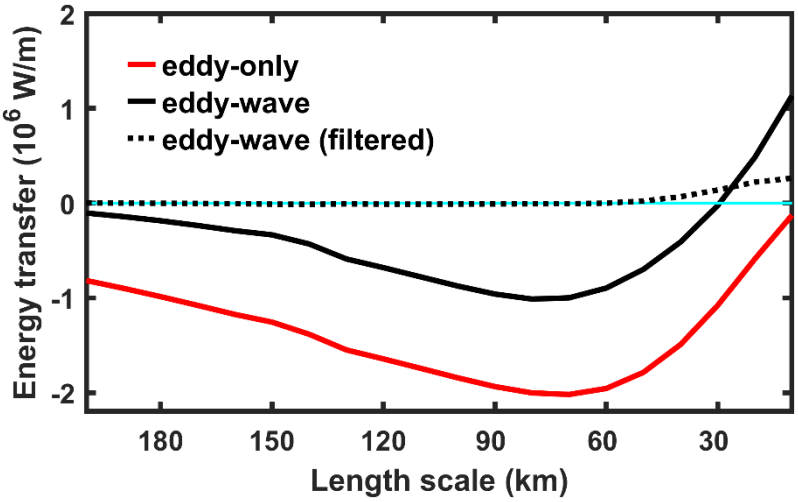

FIG. 7. Time-mean and horizontally integrated energy transfer across length scales at a depth of 5 m for the eddy-only case, the eddy-wave case, and the IW field of the eddy-wave case after Lagrangian filtering.

However, it is important to note that the diagnosed energy transfer is not necessarily attributable solely to cross-scale energy transfers. As emphasized by Kafiabad et al. (2019), Savva et al. (2021), and Cox et al. (2023), the spreading of IW energy in wavenumber space can also result from wave scattering processes, which do not involve direct energy transfer. Therefore, while our results indicate enhanced forward energy transfer in the eddy-wave case, this analysis alone cannot fully distinguish between actual energy transfer and spectral energy redistribution due to scattering. Nonetheless, the consistency of our findings across two independent diagnostic frameworks (i.e., the coarse-graining method and the MS-EVA approach) adds confidence to the robustness of our analysis. Both methods, despite their inherent limitations, reveal obvious signatures of enhanced forward energy transfer. This suggests that even if scattering contributes to the observed spectral patterns, genuine cross-scale energy transfer between eddies and IWs plays a significant role.

Fig. 8 shows the distribution of energy transfer over depth and length scale. In the eddy-only case, energy transfer is predominantly inverse and its magnitude is decreasing with depth. The eddy-wave case exhibits two local minima, indicating stronger inverse energy transfers. The first minimum, located within the mixed layer, aligns with previous findings that submesoscale processes can drive inverse energy cascades (Schubert et al., 2020; Srinivasan et

Accepted for publication in *Journal of Physical Oceanography*. DOI 10.1175/JPO-D-25-0199.1

al., 2023; Barkan et al., 2024). This suggests that the observed inverse transfer likely reflects the energetic role of submesoscale processes in feeding mesoscale flows or in the merging of smaller eddies into larger ones, both of which are active in the upper ocean. The difference between the two cases (Fig. 8c) shows that the inclusion of IWs enhances the forward energy cascade in the upper ocean (0-200 m) but promotes an enhanced inverse cascade at deeper depths (200-500 m) for large and intermediate length scales.

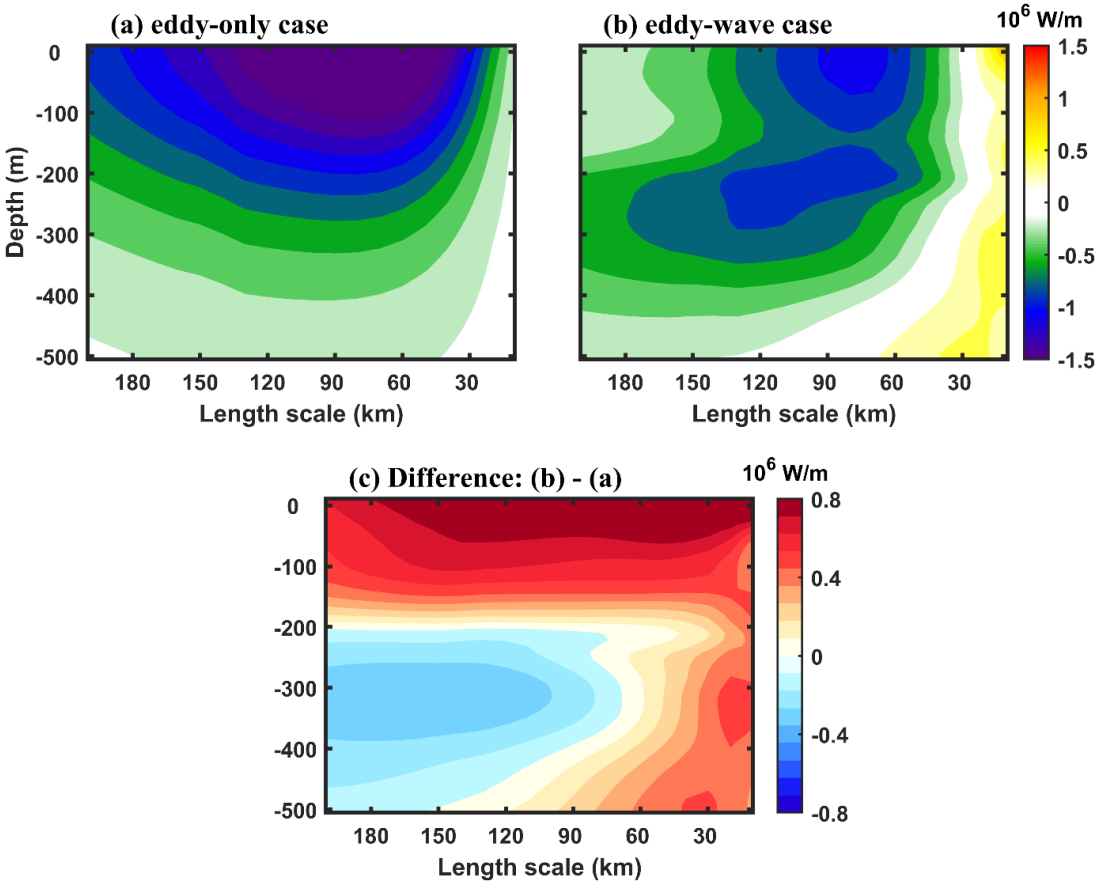

FIG. 8. Time-mean and horizontally integrated energy transfer over depth and length scale for (a) the eddy-only case, (b) the eddy-wave case, and (c) their difference (eddy-wave minus eddy-only).

One possible contributor to the second minimum near 250-m depth is wave energy reabsorption by mesoscale eddies. To demonstrate this, we analyze temporal energy transfers using the MS-EVA method (Fig. 9). The results show that energy transfer between mesoscale eddies and submesoscale motions (TK01) is predominantly inverse and its magnitude decreases with depth, suggesting it cannot explain the local enhancement near 250 m depth. In contrast, energy transfer between mesoscale eddies and IWs (TK02) peaks in inverse transfer around 250 m depth, indicating that IW reabsorption may explain the second local minimum. We note, however, that Fig. 8 reflects spatial transfers. Temporal upscale transfer does not necessarily imply a wavenumber-space cascade. Nevertheless, the significant TK02 near the

Accepted for publication in *Journal of Physical Oceanography*. DOI 10.1175/JPO-D-25-0199.1

pycnocline offers a possible explanation for the enhanced spatial inverse transfer, though the link between spatial and temporal transfers should be interpreted cautiously.

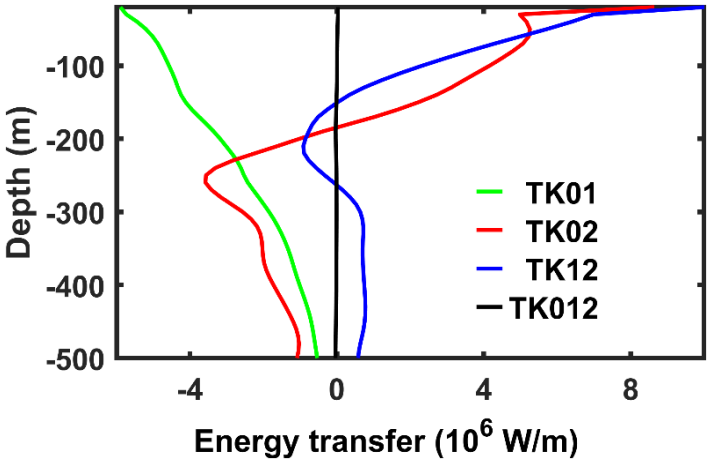

FIG. 9. Time-mean and horizontally integrated temporal energy transfer of the eddy-wave case in Eulerian coordinates. Windows [0], [1], and [2] represent mesoscale eddies, submesoscale motions, and IWs, respectively. TK01, TK02, and TK12 denote energy transfers between window pairs, with positive values indicating energy transfer from the left-numbered to the right-numbered window. TK012 represents the transfer from mesoscale-submesoscale interactions (windows [0] and [1]) to IWs (window [2]).

To further analyze detailed temporal energy transfer, Fig. 10(a) shows the vertical distributions of the transfer terms for the eddy-wave case in both Eulerian and Lagrangian coordinates. The transfers are negligible in the eddy-only and wave-only cases (not shown), so the analysis focuses on the eddy-wave case where both components coexist. The patterns in Fig. 10(a) show clear depth dependence. To better resolve associated energy distribution, frequency spectra at two representative depths are shown in Fig. 10(b). Despite a reversal of the energy transfer direction with depth (Fig. 10a), the energy spectra retain broadly similar characteristics. The most noticeable spectral discrepancy occurs in the submesoscale range between Eulerian and Lagrangian coordinates, whereas TK02 shows substantial variation and TK12 shows comparatively minor changes between these two coordinates. These results highlight that energy spectrum and transfers describe different aspects of the flow. Energy spectrum reflects the distribution of energy intensity, whereas the underlying flow structures can differ (Yu et al. 2021; Shakespeare et al. 2021). Processes such as advection, vertical transport, buoyancy conversion, and dissipation also influence energy intensity, while energy transfer is strongly influenced by phase relationships of the flow components and nonlinear triadic interactions, which are more sensitive to coordinate choice. Recent Eulerian-Lagrangian comparisons also show that similar energy spectra may originate from distinct flow structures and dynamics (Caspar-Cohen et al. 2022; Zhang et al. 2024; Caspar-Cohen et al. 2025).

Accepted for publication in *Journal of Physical Oceanography*. DOI 10.1175/JPO-D-25-0199.1

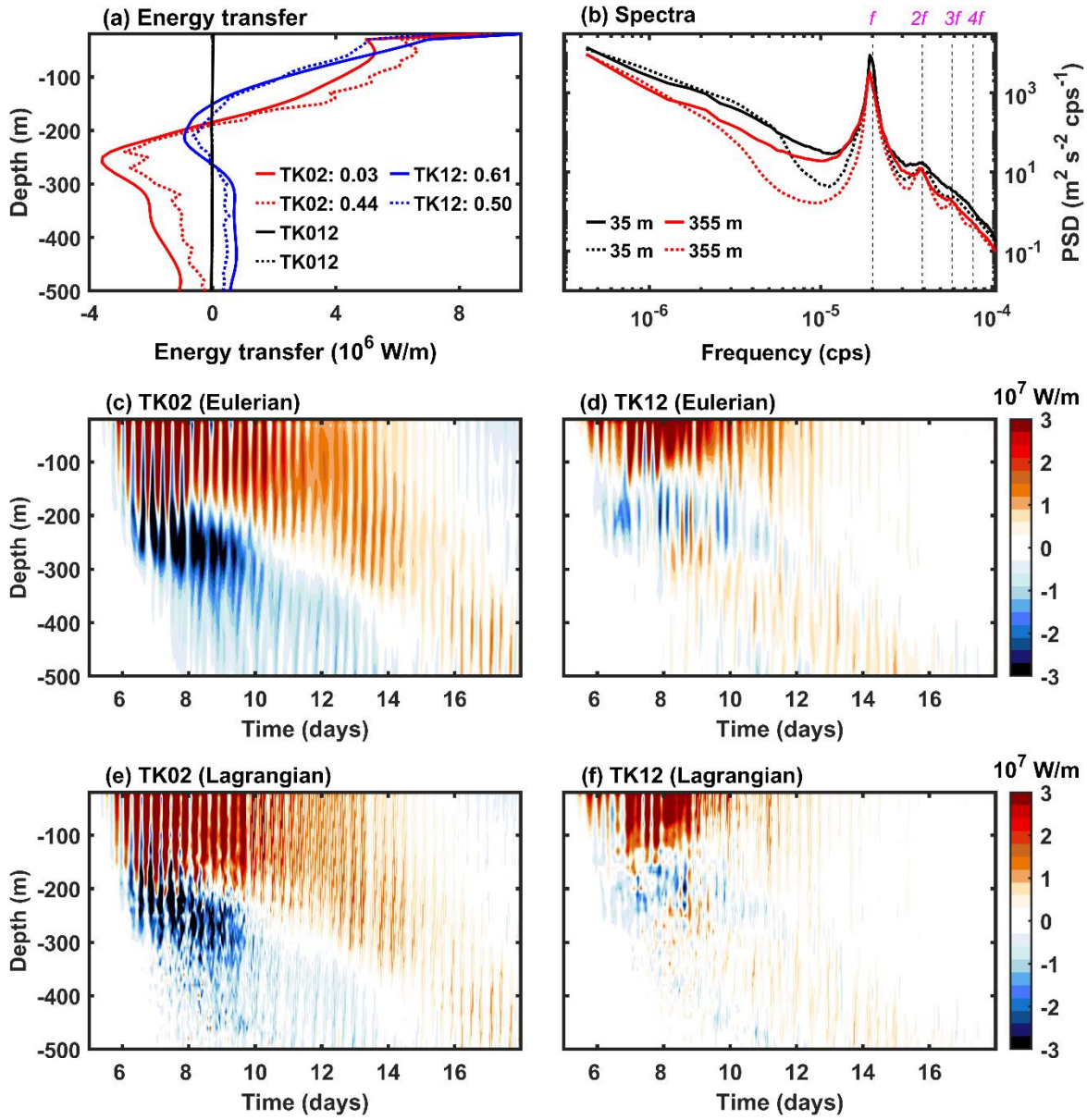

FIG. 10. (a) Time-mean and horizontally integrated temporal energy transfer, with vertically integrated values of the respective profiles indicated in the legend with a unit of GW, and (b) kinetic energy spectra at 35 m and 355 m in Eulerian (solid lines) and Lagrangian (dotted lines) coordinates. Distributions of TK02 and TK12 in Eulerian coordinates are shown in (c) and (d), respectively. (e) and (f) are respectively the same as (c) and (d) but in Lagrangian coordinates.

Next, we quantitatively analyze energy transfers in Fig. 10(a). TK012 remains near zero in both coordinates, indicating that interaction between mesoscale and submesoscale motions does not contribute significantly to IW energy. In the Eulerian coordinate, the forward energy transfer from mesoscale eddies in the upper layer and the reverse transfer to mesoscale eddies in the lower layer nearly cancel each other out, with a vertically integrated value of 0.03 GW. Nevertheless, the absolute magnitudes of these transfers are still much larger than those associated with submesoscale motions, indicating the importance of mesoscale eddies. In contrast, in the Lagrangian coordinate, the net contributions from mesoscale and submesoscale

Accepted for publication in *Journal of Physical Oceanography*. DOI 10.1175/JPO-D-25-0199.1

eddies are comparable (0.44 GW vs. 0.50 GW), with mesoscale energy transfer enhanced in the upper 200 m and reduced negative transfer below. From a more rigorous IW definition perspective, the Eulerian framework underestimates TK02 and slightly overestimates TK12, likely due to its overestimation of submesoscale motions.

The depth-time distribution of TK02 (Figs. 10c, 10e) shows bidirectional energy transfer, with predominantly positive values within the mixed layer, consistent with previous studies (Balwada et al. 2022; Qiu et al. 2022; Liu et al. 2023). In contrast, negative values in the pycnocline indicate reabsorption of IW energy by mesoscale eddies. The Lagrangian result shows similar patterns, confirming the robustness of this structure. TK12 (Figs. 10d, 10f) exhibits analogous behavior, with energy transfer from submesoscale motions to IWs in the mixed layer and reverse transfer below. Such wave energy reabsorption has also been reported in earlier works (Kunze et al. 1995; Nagai et al. 2015; Shakespeare & Hogg 2017, 2018; Taylor & Straub 2020). However, the physical context examined here is different. For example, Nagai et al. (2015) focused on spontaneously generated NIWs, which produced only weak net energy transfers. In contrast, NIWs in our simulations are generated by external forcing, which leads to more substantial energy transfers. Kunze et al. (1995) identified reabsorption of wave energy in critical layers, while Shakespeare & Hogg (2017, 2018) highlighted counter-interactions between downward/upward propagating IWs and geostrophic vertical shear. Both mechanisms appear in our simulations and we will further explore how they operate under externally forced conditions in the following Section 3d.

d. Mechanism underlying the Energy Transfers

To understand these dynamics, this section explores potential mechanisms driving the observed energy transfers. We first analyze basic dynamical properties of the flow field. The relative vorticity (ζ), strain rate (St), vertical shear (Sh), and Okubo-Weiss (OW) parameter (Okubo 1970; Weiss 1991) are calculated as

$$\zeta = \frac{\partial v}{\partial x} - \frac{\partial u}{\partial y}, \tag{3}$$

$$St = \sqrt{\left(\frac{\partial u}{\partial x} - \frac{\partial v}{\partial y}\right)^2 + \left(\frac{\partial v}{\partial x} + \frac{\partial u}{\partial y}\right)^2}, \tag{4}$$

$$Sh = \sqrt{\left(\frac{\partial u}{\partial z}\right)^2 + \left(\frac{\partial v}{\partial z}\right)^2}, \tag{5}$$

$$OW = St_g^2 - \zeta_g^2, \tag{6}$$

Accepted for publication in *Journal of Physical Oceanography*. DOI 10.1175/JPO-D-25-0199.1

where St_g and ζ_g denote geostrophic strain rate and relative vorticity, respectively. Fig. 11 presents vertical profiles of these variables. The mean relative vorticity (Fig. 11a) is predominantly negative, implying anticyclonic dominance. The strain field (Fig. 11b) is mainly eddy-induced in the upper ocean, but wave-induced at greater depths, indicating a shift in the dominant dynamic. Strong vertical shear and OW values (Figs. 11c-11d) appear within the mixed layer and near the 200 m depth in the pycnocline.

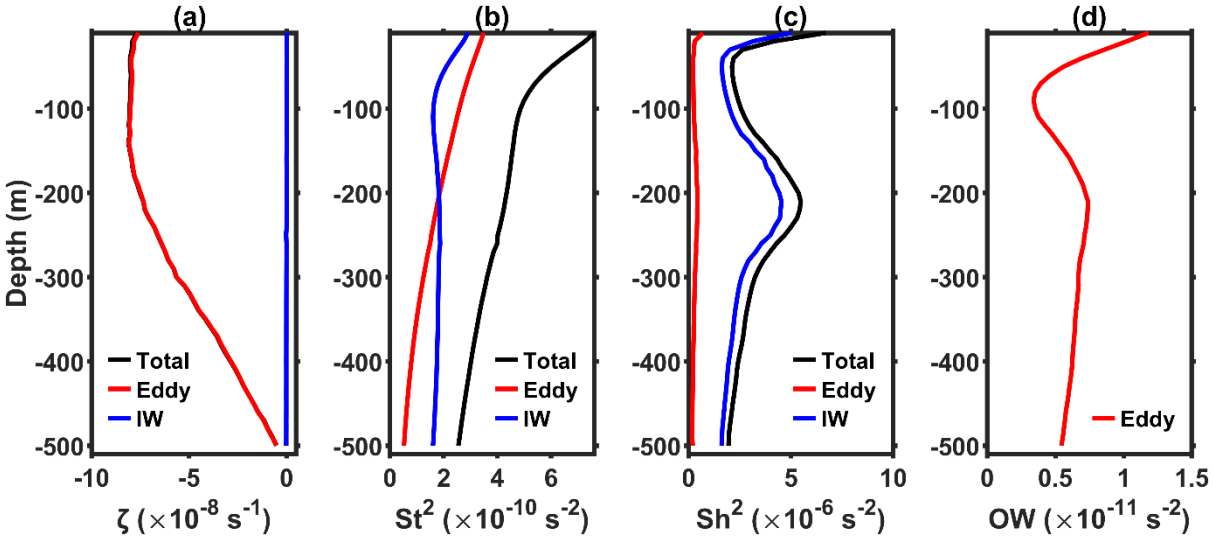

FIG. 11. Vertical profiles of flow diagnostics of the eddy-wave case in the Lagrangian coordinate. Horizontally and temporally averaged (a) relative vorticity; (b) strain squared; (c) vertical shear squared; and (d) Okubo-Weiss (OW) parameter.

For the observed energy transfers, we consider three key mechanisms. (1) Wave capture mechanism (Bühler & McIntyre 2005; Jing et al. 2018): initially isotropic IW vectors produce little net energy transfer with the geostrophic flow; when wave capture plays a role, geostrophic strain modifies IW propagation, aligning wave vector direction toward that predicted from wave capture theory and thereby enabling stronger energy transfer from mesoscale eddies to IWs. (2) Critical-layer effect (Kunze et al. 1995; Chen et al. 2023; Thomas et al. 2024): as IWs propagate downward, they may encounter the critical layer, causing them to stall. Trapped NIW energy can cascade inversely to the background flow, cascade forward to higher-frequency IWs, or enhance shear and turbulent mixing. (3) Counter-interactions between downward/upward propagating IWs and geostrophic vertical shear (Shakespeare & Hogg 2017, 2018): downward propagating IWs gain energy through interaction with geostrophic vertical shear, but after reflection upward propagating IWs encounter opposite shear and return energy to the background flow. This process further strengthens the bidirectional energy transfer. We further discuss each mechanism below.

Accepted for publication in *Journal of Physical Oceanography*. DOI 10.1175/JPO-D-25-0199.1

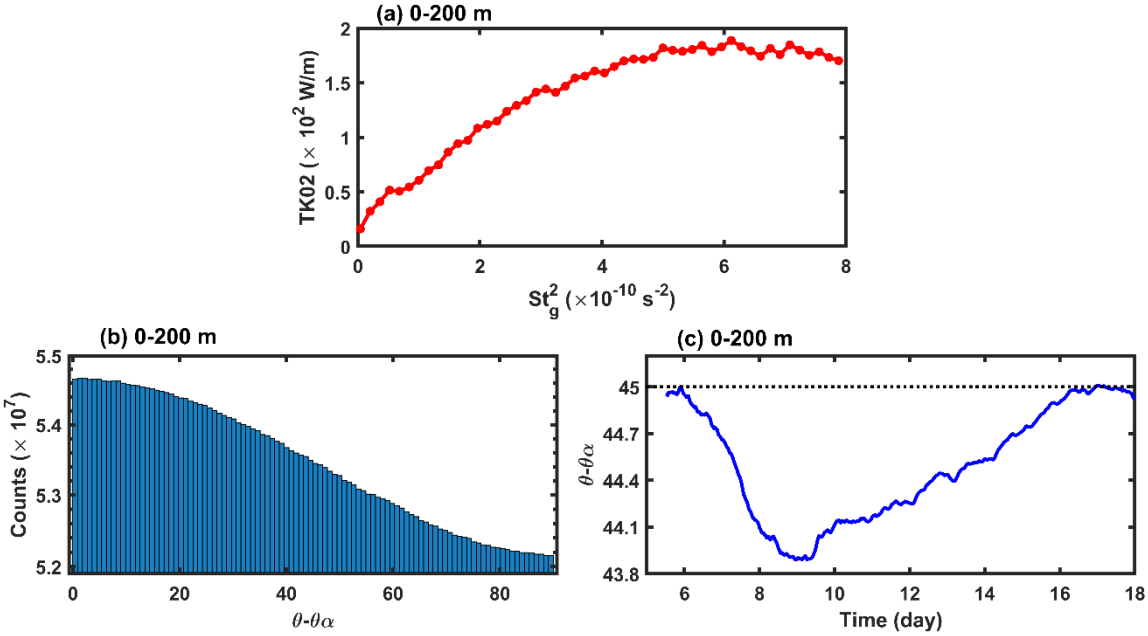

FIG. 12. Relationships between geostrophic strain and energy transfer of the eddy-wave case in the Lagrangian coordinate. (a) Mean TK02 versus geostrophic strain squared (St_g^2). (b) Histogram of the angle difference (θ-θ_α) between the IW horizontal wavevector and the theoretical angle. (c) Temporal evolution of the volume-averaged θ-θ_α.

We also calculate TK02 with the increase of the strain rate (Fig. 12a). Energy transfer increases with strain rate, indicating that geostrophic strain enhances forward energy transfer. Following Jing et al. (2018), we compute two diagnostic angles: the azimuth of the horizontal IW vector θ and the theoretical alignment angle θ_α predicted by wave capture. The azimuth θ is calculated as

$$tan2\theta = 2\mathrm{Re}(\Phi_{uv})/(\Phi_{uu} - \Phi_{vv}), \tag{7}$$

where Φ_{uu} and Φ_{vv} are the autospectra of the horizontal velocities, and Φ_{uv} is their cross-spectrum. The theoretical angle θ_α is written as

$$\theta_\alpha = arctan[-(U_x + \lambda)/V_x], \tag{8}$$

where U_x and V_x are the horizontal velocity gradients of mesoscale eddies, and λ is the half square root of the OW parameter. Under isotropy, θ-θ_α is uniformly distributed with a mean of 45°, whereas active wave capture results in smaller values. As shown in Figs. 12(b-c), θ-θ_α slightly decreases during the storm, while before and after the storm the waves are nearly isotropic. This shows a weak tendency consistent with the wave capture mechanism. This small reduction of θ-θ_α is similar to the result of Jing et al. (2018). However, in contrast to Jing et al. (2018) who found that strain-dominated (positive OW) regions favor energy transfer, we observe positive OW signals both in the mixed layer and near 200 m depth, yet the latter

Accepted for publication in *Journal of Physical Oceanography*. DOI 10.1175/JPO-D-25-0199.1

corresponds to reverse transfer. This difference likely arises from strong storm-induced IWs. Below 200 m depth, IW strain exceeds geostrophic strain (Fig. 11b), implying that there is insufficient geostrophic strain to reorient the wave vector.

The inverse energy transfer near 250 m depth can be attributed to critical layer reabsorption. Dominant negative vorticity (Fig. 11a) indicates prevailing anticyclonic eddies, whose reduced effective Coriolis frequency facilitates downscale energy cascade and potential wave energy absorption near the eddy bases. To assess whether this reabsorption is linked to NIW stalling within the critical layer, we apply a modified MS-EVA windowing scheme: window [0] for sub-inertial motions (<0.7*f*), window [1] for NIWs (0.7*f*-1.3*f*), and window [2] for super-inertial IWs (>1.3*f*). The inverse transfer previously diagnosed between mesoscale eddies and IWs in the pycnocline primarily arises from the energy transfer between sub-inertial motions and NIWs (Fig. 13). It is consistent with the critical-layer dynamics, where NIW energy partly returns to the background flow. A clear enhancement of the NIW vertical wavenumber around 250 m depth also supports the presence of a critical layer (not shown). The inferred critical layer agrees with previous studies, e.g., Zhang et al. (2018) reported NIW dissipation near the critical layer at ~ 200 m depth, Xu et al. (2022) observed NIWs trapped at depths of 200-315 m, and Li et al. (2022) identified critical layers occurring between 350-650 m. Enhanced shear in this layer mainly arises from near-inertial shear, consistent with Chen et al. (2023).

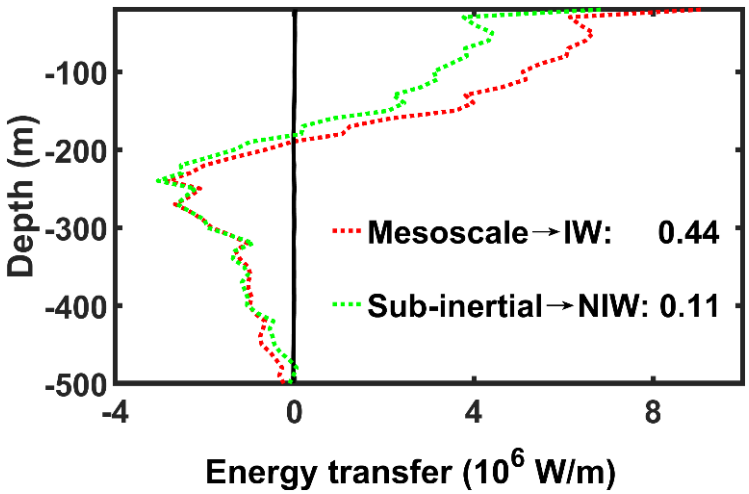

FIG. 13. Time-mean and horizontally integrated energy transfer of the eddy-wave case in the Lagrangian coordinate, with vertically integrated values of each profile indicated in the legend with a unit of GW. The red dotted curve is also the one from Fig. 10(a). The green dotted curve shows the energy transfer from sub-inertial motions to NIWs using a new windowing scheme: windows [0], [1], and [2] correspond to sub-inertial motions, NIWs, and high-frequency IWs, respectively.

Accepted for publication in *Journal of Physical Oceanography*. DOI 10.1175/JPO-D-25-0199.1

Interactions between downward/upward propagating IWs and geostrophic vertical shear are also found to play a role in the energy transfer. By examining the variation of TK02 with geostrophic vertical shear, we find that TK02 intensifies with increasing shear (Fig. 14a). To further explore their connection, downward and upward propagating IWs are separated using a Fourier transform in the vertical direction. It is shown that both forward and inverse transfers grow with increasing IW speed (Figs. 14b-14c). However, strong downward propagating IWs favor forward transfer, whereas strong upward-propagating IWs favor inverse transfer. This agrees with Shakespeare & Hogg (2017, 2018), who showed that downward propagating IWs gain energy from the background shear, while reflected upward propagating IWs return energy to the background flow due to the opposite shear interaction. A key distinction is that they examined spontaneously generated IWs that travel nearly with the mean flow and thus experience little horizontal straining effects. In contrast, the storm-generated IWs here propagate differently from the background flow, interact more strongly with the horizontal strain, and consequently enhance energy transfer.

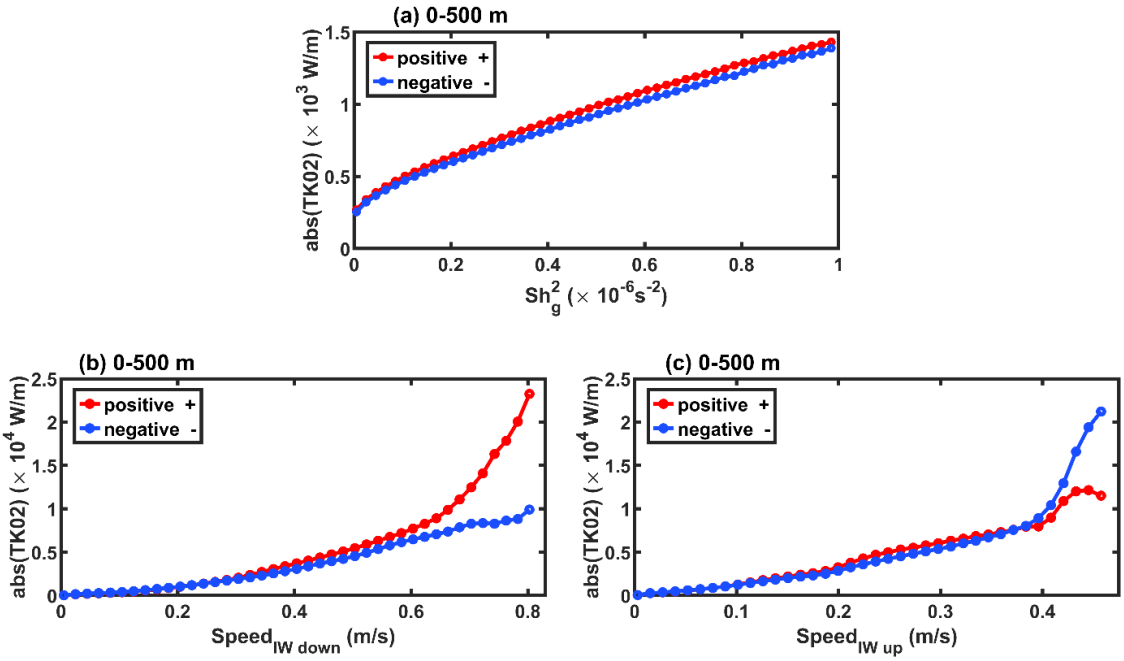

FIG. 14. Variations of the absolute energy transfer of the eddy-wave case in the Lagrangian coordinate. (a) Variations of abs(TK02) with geostrophic vertical shear squared (Sh_g^2). (b) Variations of abs(TK02) with downward propagating IW speed (velocity magnitude). (c) The same as (b), but for upward propagating IWs.

e. Formation of a GM-like spectrum in the Southern Ocean

The Southern Ocean is an eddying ocean forced by strong winds yet with weak internal tides (Savage et al. 2017), and thus is an ideal place for testing the formation of a GM-like

Accepted for publication in *Journal of Physical Oceanography*. DOI 10.1175/JPO-D-25-0199.1

spectrum noted in the simulations. The mooring dataset contains velocity records from 906 current meters in the Southern Ocean spanning years 1975-2010, which is assembled by the Buoy Group at the Oregon State University. Moorings in coastal waters with depths shallower than 500 m or within 50 km off the shoreline (yellow dots in Fig. 15) are excluded, and only the red dots in Fig. 15 are used for analysis. Then, each current meter record is demeaned and detrended, and 7-day low-pass filtering is applied to obtain mesoscale velocities while band-pass filtering is used to obtain NIW velocities (0.85f-1.15f). If there are missing values, the time series are split, and velocity records shorter than 21 days or with sampling intervals greater than 1 hour are removed.

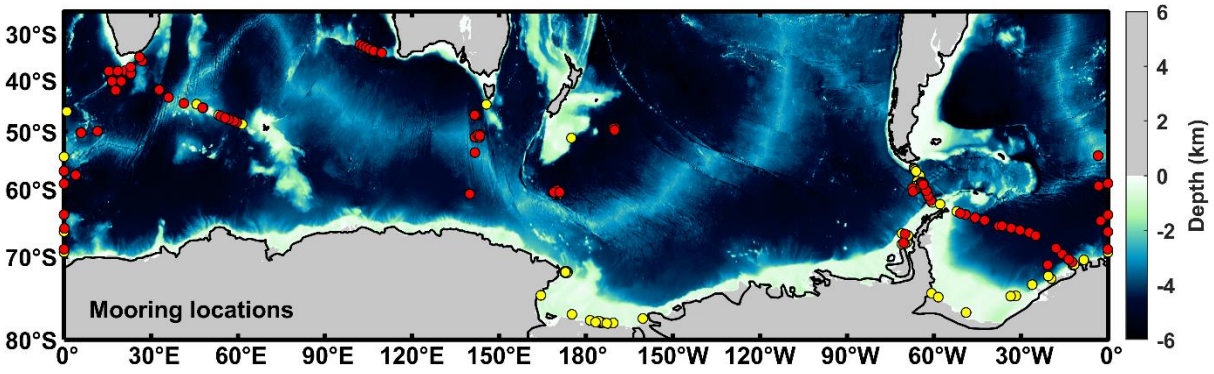

FIG. 15. Mooring locations in the Southern Ocean, with the near-coast or shallow-water ones (yellow dots) excluded for analysis, and only the red ones used in this study.

Even though the Southern Ocean has overall weak internal tides, to further minimize the influence of internal tides, a threshold is set that if the maximum diurnal or semidiurnal current speed in a time series exceeds 6 cm/s, the time series is removed. The resulting time series are divided into segments of 10 days in length, with those less than 10 days discarded. This results in a total of 6337 segments. These 10-day segments are used for power spectral analysis. Note that the Southern Ocean has an inertial period of about 0.6 days.

Depths of the data segments are shown in Fig. 16(a), which range from 120 m to 5230 m. Most of the data segments have a maximum NIW speed of less than 10 cm/s (Fig. 16b) and a maximum mesoscale eddy speed of less than 30 cm/s (Fig. 16c). We define the situation of "strong NIWs" with maximum NIW speed greater than 9 cm/s, which contains 217 data segments. Then, two situations are analyzed to show the effect of mesoscale eddies in diffusing NIW energy. One situation is "weak eddies and strong NIWs" with a maximum mesoscale eddy speed less than 6 cm/s, which contains 51 data segments. The other situation is "strong eddies and strong NIWs" with a maximum mesoscale eddy speed greater than 30 cm/s, which contains 49 data segments.

Accepted for publication in *Journal of Physical Oceanography*. DOI 10.1175/JPO-D-25-0199.1

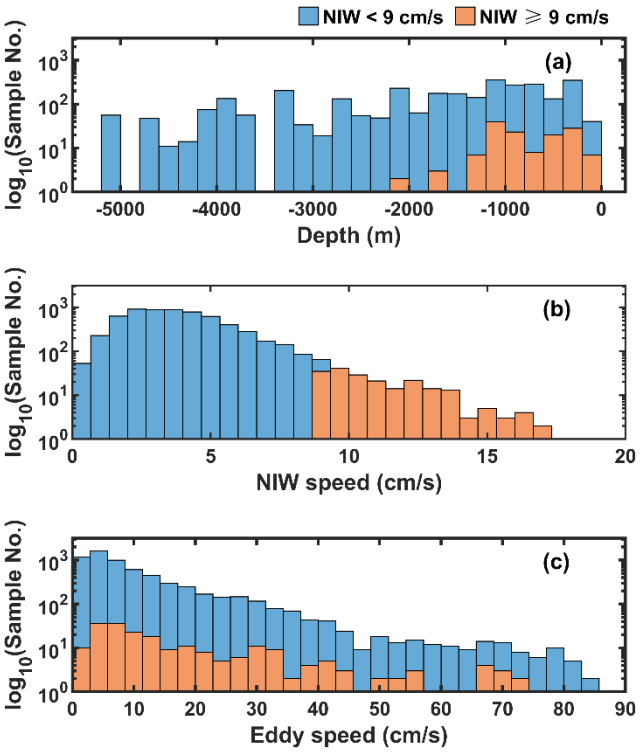

FIG. 16. Statistics of mooring observations from the Southern Ocean. Logarithms of the sample (10-day data segment) number for (a) different depths, maximum (b) NIW, and (c) eddy speeds (velocity magnitude) in the data segments. The blue portion of each stacked bar indicates the subset of data with NIW speed < 9 cm/s, whereas the orange portion indicates the subset with NIW speed ≥ 9 cm/s.

The averaged spectra of these two situations are shown in Figs. 17(a-b). In the situation of weak eddies, the spectrum shows significant peaks at *f* and its higher harmonics (up to 3*f*, Fig. 17a), which resembles the features noted in the wave-only case of simulation (blue line in Fig. 5a). The difference is that the wave-only case of simulation has no eddies at all, while in a real eddying ocean, mesoscale eddies are always present, albeit relatively weak. The eddy energy at the low-frequency end of the spectrum is comparable to that of the NIW energy. However, for the "strong eddies and strong NIWs" situation in Fig. 17(b), the eddy energy is more than one order of magnitude stronger than the NIW energy and the higher harmonics of *f* disappear, indicating that mesoscale eddies are capable of redistributing NIW energy across the spectrum. The resulting averaged spectrum closely resembles the GM spectrum, as has been noted in the eddy-wave case of simulation (solid black line in Fig. 5a). Considering the idealized setups in the simulations, it is quite remarkable that the effects of mesoscale eddies in facilitating the formation of a GM-like spectrum noted in the simulations can be observed in the Southern Ocean.

Accepted for publication in *Journal of Physical Oceanography*. DOI 10.1175/JPO-D-25-0199.1

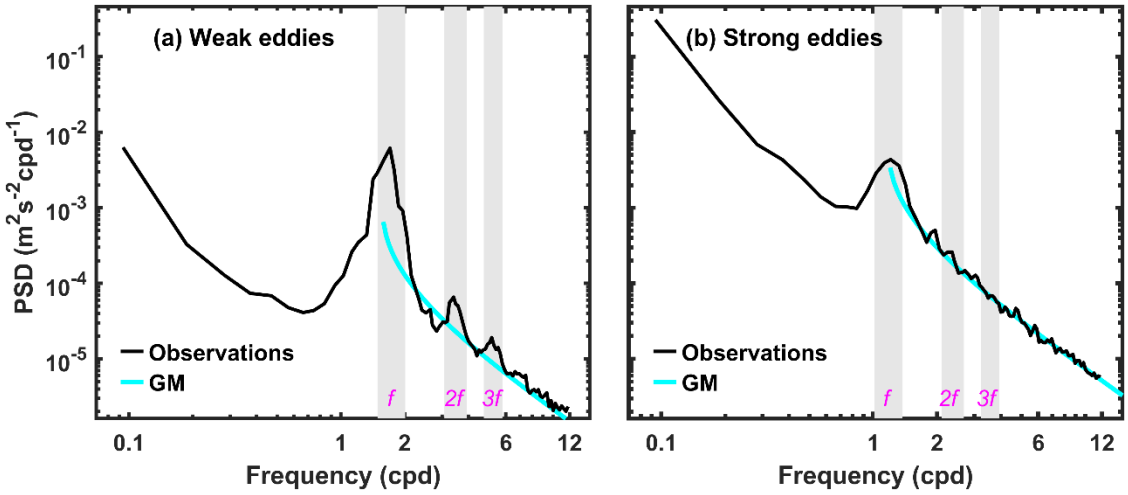

FIG. 17. In-situ observations of IW spectra in the Southern Ocean. Averaged frequency spectra for situations of (a) "weak eddies and strong NIWs" and (b) "strong eddies and strong NIWs".

4. Conclusions

An idealized reentrant channel model is utilized to study the formation of a GM-like spectrum by high-frequency winds blowing over an eddying ocean. High-frequency winds generate NIWs, which subsequently interact with mesoscale eddies and submesoscale motions to produce a GM-like spectrum. During the formation of this spectrum, in the Eulerian coordinate, the net energy transfer from mesoscale eddies is small due to near cancellation between the forward transfer in the upper layer and the reverse transfer in the lower layer; however, the absolute magnitudes of these transfers are still much larger than those associated with submesoscale motions. In contrast, in the Lagrangian coordinate, the contributions from mesoscale and submesoscale eddies are of comparable magnitude, implying the equal importance of direct extraction and stimulated cascades in generating a GM-like spectrum. This implies that, from a more rigorous IW definition perspective (Lagrangian coordinate), the direct extraction likely plays a more important role in energy transfer than previously recognized in Eulerian coordinates.

In the upper mixed layer, mesoscale eddies transfer energy to IWs, whereas in the pycnocline, a portion of IW energy is transferred back to mesoscale eddies. This reverse transfer reduces the amount of wind-induced NIW energy that penetrates into the deeper ocean. Wind-induced NIWs are generally believed to dissipate most of their energy within the surface layer through shear instability and mixing, allowing only a small fraction to radiate downward into the ocean interior (e.g., Furuichi et al. 2008; Zhai et al. 2009). The reabsorption of NIW

Accepted for publication in *Journal of Physical Oceanography*. DOI 10.1175/JPO-D-25-0199.1

energy by mesoscale eddies in the pycnocline may further limit the downward propagation of this energy, especially during the passage of a storm.

Our results also highlight the important role of wave capture, critical layer, and counter-interaction between downward/upward propagating IWs and geostrophic vertical shear in mediating energy transfer. The azimuthal distribution of IW vectors exhibits a tendency consistent with predictions of the wave-capture mechanism, leading to enhanced energy transfer from mesoscale eddies to IWs. NIW energy reabsorption by the background flow in the critical layer can explain reverse transfer in the pycnocline. Counter-interactions between downward/upward propagating IWs and vertical shear also contribute to the bidirectional energy transfer. Downward propagating IWs gain energy from the background shear, while reflected upward propagating IWs return energy back to the background flow due to the opposite shear interaction.

The simulated effect of eddies in facilitating the formation of a GM-like spectrum is also observed from current meter records in the eddying Southern Ocean with weak internal tides. Considering the idealized numerical setups, it is remarkable that this effect can be observed in a complicated real ocean. Overall, both simulations and observations show that a GM-like spectrum can be generated by wind forcing over an eddying ocean. This is complementary to our previous study that tidal forcing with topography can generate a GM-like IW spectrum (Chen et al., 2019). Considering that mesoscale eddies and wind forcing are ubiquitous in the upper ocean while tidal forcing mainly occurs in the deep ocean, these results together might explain why a GM-like IW spectrum is usually observed in the ocean.

Acknowledgments.

This work was jointly supported by the National Natural Science Foundation of China (Nos. 42130404, 42576015, 42176025, 42276022, and 42206012), the National Key R&D Program of China (2023YFF0805300), the Oceanic Interdisciplinary Program of Shanghai Jiao Tong University (SL2023MS016), the South China Sea Institute of Oceanology (SCSIO2023QY02), the LTO Independent Research Program (LTOZZ2205), and the Science and Technology Projects of Guangzhou (No. 2024A04J6273). The numerical simulations are supported by the High Performance Computing Division and HPC managers of Wei Zhou and Dandan Sui in the South China Sea Institute of Oceanology.

Accepted for publication in *Journal of Physical Oceanography*. DOI 10.1175/JPO-D-25-0199.1

Data Availability Statement.

The Massachusetts Institute of Technology general circulation model (MITgcm) is publicly available at https://mitgcm.org/source-code/. Our model configurations and input data can be accessed at https://figshare.com/articles/dataset/Zhang_et_al_rar/26132677. Mooring current meter data are available for download at https://cmrecords.net/index.html. The code for the MS-EVA is downloaded from http://www.ncoads.cn/article/show/63.aspx, while the code of the coarse-graining method is from https://github.com/husseinaluie/FlowSieve. The codes for the Lagrangian Transformation and Filtering are obtained from https://github.com/angus-g/lagrangian-filtering.

REFERENCES

[1]. Alford, M. H., MacKinnon, J. A., Simmons, H. L., & Nash, J. D. (2016). Near-inertial internal gravity waves in the ocean. Annual review of marine science, 8(1), 95-123. https://doi.org/10.1146/annurev-marine-010814-015746

[2]. Aluie, H., Hecht, M., & Vallis, G. K. (2018). Mapping the energy cascade in the North Atlantic Ocean: The coarse-graining approach. Journal of Physical Oceanography, 48(2), 225-244. https://doi.org/10.1175/JPO-D-17-0100.1

[3]. Arbic, B.K., Alford, M. H., Ansong, J. K., Buijsman, M. C., Ciotti, R. B., Farrar, J. T., et al., 2018: A primer on global internal tide and internal gravity wave continuum modeling in HYCOM and MITgcm. In "New Frontiers in Operational Oceanography", E. Chassignet, A. Pascual, J. Tintoré, and J. Verron, Eds., GODAE OceanView, 307-392, doi:10.17125/gov2018.ch13

[4]. Balwada, D., Xie, J. H., Marino, R., & Feraco, F. (2022). Direct observational evidence of an oceanic dual kinetic energy cascade and its seasonality. Science Advances, 8(41), eabq2566. https://doi.org/10.1126/sciadv.abq2566

[5]. Barkan, R., Winters, K. B., & McWilliams, J. C. (2017). Stimulated imbalance and the enhancement of eddy kinetic energy dissipation by internal waves. Journal of Physical Oceanography, 47(1), 181-198. https://doi.org/10.1175/JPO-D-16-0117.1

[6]. Barkan, R., Srinivasan, K., Yang, L., McWilliams, J. C., Gula, J., & Vic, C. (2021). Oceanic mesoscale eddy depletion catalyzed by internal waves. Geophysical Research Letters, 48(18), e2021GL094376. https://doi.org/10.1029/2021GL094376

[7]. Barkan, R., Srinivasan, K., & McWilliams, J. C. (2024). Eddy-Internal Wave Interactions: Stimulated Cascades in Cross-scale Kinetic Energy and Enstrophy Fluxes. Journal of Physical Oceanography. https://doi.org/10.1175/JPO-D-23-0191.1

[8]. Bühler, O., & McIntyre, M. E. (2005). Wave capture and wave-vortex duality. Journal of

Accepted for publication in *Journal of Physical Oceanography*. DOI 10.1175/JPO-D-25-0199.1

Fluid Mechanics, 534, 67-95. https://doi.org/10.1017/S0022112005004374

[9]. Caspar-Cohen, Z., Ponte, A., Lahaye, N., Carton, X., Yu, X., & Gentil, S. L. (2022). Characterization of internal tide incoherence: Eulerian versus Lagrangian perspectives. Journal of Physical Oceanography, 52(6), 1245-1259. https://doi.org/10.1175/JPO-D-21-0088.1

[10]. Caspar-Cohen, Z., Ponte, A., Lahaye, N., Zaron, E. D., Arbic, B. K., Yu, X., LeGentil, S., & Menemenlis, D. (2025). Combining surface drifters and high resolution global simulations enables the mapping of internal tide surface energy. Scientific Reports, 15(1), 10672. https://doi.org/10.1038/s41598-025-92662-w

[11]. Charney, J. G. (1971). Geostrophic turbulence. Journal of Atmospheric Sciences, 28(6), 1087-1095. https://doi.org/10.1175/1520-0469(1971)028<1087:GT>2.0.CO;2

[12]. Chen, Z., Chen, S., Liu, Z., Xu, J., Xie, J., He, Y., & Cai, S. (2019). Can tidal forcing alone generate a GM-like internal wave spectrum?. Geophysical Research Letters, 46(24), 14644-14652. https://doi.org/10.1029/2019GL086338

[13]. Chen, Z., Yu, F., Chen, Z., Wang, J., Nan, F., Ren, Q., Hu, Y., Cao, A., & Zheng, T. (2023). Downward propagation and trapping of near-inertial waves by a westward-moving anticyclonic eddy in the subtropical northwestern Pacific Ocean. Journal of Physical Oceanography, 53(9), 2105-2120. https://doi.org/10.1175/JPO-D-22-0226.1

[14]. Cox, M. R., Kafiabad, H. A., & Vanneste, J. (2023). Inertia-gravity-wave diffusion by geostrophic turbulence: the impact of flow time dependence. Journal of Fluid Mechanics, 958, A21. https://doi.org/10.1017/jfm.2023.83

[15]. Delpech, A., Barkan, R., Srinivasan, K., McWilliams, J. C., Arbic, B. K., Siyanbola, O. Q., & Buijsman, M. C. (2024). Eddy-internal wave interactions and their contribution to cross-scale energy fluxes: A case study in the California current. Journal of Physical Oceanography, 54(3), 741-754. https://doi.org/10.1175/JPO-D-23-0181.1

[16]. Dong, W., Bühler, O., & Smith, K. S. (2023). Geostrophic eddies spread near-inertial wave energy to high frequencies. Journal of Physical Oceanography, 53(5), 1311-1322. https://doi.org/10.1175/JPO-D-22-0153.1

[17]. Ferrari, R., & Wunsch, C. (2009). Ocean circulation kinetic energy: Reservoirs, sources, and sinks. Annual Review of Fluid Mechanics, 41(1), 253-282. https://doi.org/10.1146/annurev.fluid.40.111406.102139

[18]. Fu, L. L. (1981). Observations and models of inertial waves in the deep ocean. Reviews of Geophysics, 19(1), 141-170. https://doi.org/10.1029/RG019i001p00141

[19]. Furuichi, N., Hibiya, T., & Niwa, Y. (2008). Model-predicted distribution of wind-induced internal wave energy in the world's oceans. Journal of Geophysical Research: Oceans, 113(C9). https://doi.org/10.1029/2008JC004768

Accepted for publication in *Journal of Physical Oceanography*. DOI 10.1175/JPO-D-25-0199.1

[20]. Garrett, C., & Munk, W. (1972). Space-time scales of internal waves. Geophysical Fluid Dynamics, 3(3), 225-264. https://doi.org/10.1080/03091927208236082

[21]. Garrett, C., & Munk, W. (1975). Space-time scales of internal waves: A progress report. Journal of Geophysical Research, 80(3), 291-297. https://doi.org/10.1029/JC080i003p00291

[22]. Garrett, C., & Munk, W. (1979). Internal waves in the ocean. Annual review of fluid mechanics, 11(1), 339-369. https://doi.org/10.1146/annurev.fl.11.010179.002011

[23]. Gill, A. E. (1984). On the behavior of internal waves in the wakes of storms. Journal of physical oceanography, 14(7), 1129-1151. https://doi.org/10.1175/1520-0485(1984)014<1129:OTBOIW>2.0.CO;2

[24]. Jing, Z., Chang, P., DiMarco, S. F., & Wu, L. (2018). Observed energy exchange between low-frequency flows and internal waves in the Gulf of Mexico. Journal of Physical Oceanography, 48(4), 995-1008. https://doi.org/10.1175/JPO-D-17-0263.1

[25]. Kafiabad, H. A., Savva, M. A., & Vanneste, J. (2019). Diffusion of inertia-gravity waves by geostrophic turbulence. Journal of Fluid Mechanics, 869, R7. https://doi.org/10.1017/jfm.2019.300

[26]. Kang, D., & Fringer, O. (2010). On the calculation of available potential energy in internal wave fields. Journal of Physical Oceanography, 40(11), 2539-2545. https://doi.org/10.1175/2010JPO4497.1

[27]. Kunze, E. (1985). Near-inertial wave propagation in geostrophic shear. Journal of Physical Oceanography, 15(5), 544-565. https://doi.org/10.1175/1520-0485(1985)015<0544:NIWPIG>2.0.CO;2

[28]. Kunze, E., Schmitt, R. W., & Toole, J. M. (1995). The energy balance in a warm-core ring's near-inertial critical layer. Journal of Physical Oceanography, 25(5), 942-957. https://doi.org/10.1175/1520-0485(1995)025<0942:TEBIAW>2.0.CO;2

[29]. Liang, X.S., 2016. Canonical transfer and multiscale energetics for primitive and quasigeostrophic atmospheres. J. Atmos. Sci. 73 (11), 4439–4468. https://doi.org/10.1175/JAS-D-16-0131.1

[30]. Li, Q., Chen, Z., Guan, S., Yang, H., Jing, Z., Liu, Y., Sun, B., & Wu, L. (2022). Enhanced near-inertial waves and turbulent diapycnal mixing observed in a cold-and warm-core eddy in the Kuroshio Extension region. Journal of Physical Oceanography, 52(8), 1849-1866. https://doi.org/10.1175/JPO-D-21-0160.1

[31]. Liu, G., Chen, Z., Lu, H., Liu, Z., Zhang, Q., He, Q., et al. (2023). Energy Transfer Between Mesoscale Eddies and Near-Inertial Waves From Surface Drifter Observations. Geophysical Research Letters, 50(16), e2023GL104729. https://doi.org/10.1029/2023GL104729

Accepted for publication in *Journal of Physical Oceanography*. DOI 10.1175/JPO-D-25-0199.1

[32]. Lvov, Y. V., Polzin, K. L., & Yokoyama, N. (2012). Resonant and near-resonant internal wave interactions. Journal of Physical Oceanography, 42(5), 669-691. https://doi.org/10.1175/2011JPO4129.1

[33]. Marshall, J., Hill, C., Perelman, L., & Adcroft, A. (1997). Hydrostatic, quasi-hydrostatic, and nonhydrostatic ocean modeling. Journal of Geophysical Research: Oceans, 102(C3), 5733-5752. https://doi.org/10.1029/96JC02776

[34]. McComas, C. H., & Bretherton, F. P. (1977). Resonant interaction of oceanic internal waves. Journal of Geophysical Research, 82(9), 1397-1412. https://doi.org/10.1029/JC082i009p01397

[35]. Müller, M., Arbic, B. K., Richman, J. G., Shriver, J. F., Kunze, E. L., Scott, R. B., et al. (2015). Toward an internal gravity wave spectrum in global ocean models. Geophysical Research Letters, 42(9), 3474-3481. https://doi.org/10.1002/2015GL063365

[36]. Müller, P., Holloway, G., Henyey, F., & Pomphrey, N. (1986). Nonlinear interactions among internal gravity waves. Reviews of Geophysics, 24, 493–536. https://doi.org/10.1029/RG024i003p00493

[37]. Müller, P., McWilliams, J. C., & Molemaker, M. J. (2005). Routes to dissipation in the ocean: The 2D/3D turbulence conundrum. Marine turbulence: theories, observations and models, 397, 405.

[38]. Munk, W. H. (1981). In B. A. Warren, & C. Wunsch (Eds.), Internal waves and small-scale processes, Evolution of Physical Oceanography: Scientific Surveys in Honor of Henry Stommel, (pp. 264–291). Cambridge: The MIT Press

[39]. Nagai, T., Tandon, A., Kunze, E., & Mahadevan, A. (2015). Spontaneous generation of near-inertial waves by the Kuroshio Front. Journal of Physical Oceanography, 45(9), 2381-2406. https://doi.org/10.1175/JPO-D-14-0086.1

[40]. Niwa, Y., & Hibiya, T. (1997). Nonlinear processes of energy transfer from traveling hurricanes to the deep ocean internal wave field. Journal of Geophysical Research: Oceans, 102(C6), 12469-12477. https://doi.org/10.1029/97JC00588

[41]. Okubo, A. (1970, June). Horizontal dispersion of floatable particles in the vicinity of velocity singularities such as convergences. In Deep sea research and oceanographic abstracts (Vol. 17, No. 3, pp. 445-454). Elsevier. https://doi.org/10.1016/0011-7471(70)90059-8

[42]. Olbers, D., Willebrand, J., & Eden, C. (2012). Ocean dynamics. Springer Science & Business Media.

[43]. Polzin, K. L. (2010). Mesoscale eddy-internal wave coupling. Part II: Energetics and results from PolyMode. Journal of physical oceanography, 40(4), 789-801.. https://doi.org/10.1175/2009JPO4039.1

Accepted for publication in *Journal of Physical Oceanography*. DOI 10.1175/JPO-D-25-0199.1

[44]. Polzin, K. L., & Lvov, Y. V. (2011). Toward regional characterizations of the oceanic internal wavefield. Reviews of geophysics, 49(4). https://doi.org/10.1029/2010RG000329

[45]. Qiu, B., Nakano, T., Chen, S., & Klein, P. (2022). Bi-directional energy cascades in the Pacific Ocean from equator to subarctic gyre. Geophysical Research Letters, 49(8), e2022GL097713. https://doi.org/10.1029/2022GL097713

[46]. Rocha, C. B., Chereskin, T. K., Gille, S. T., & Menemenlis, D. (2016). Mesoscale to submesoscale wavenumber spectra in Drake Passage. Journal of Physical Oceanography, 46(2), 601-620. https://doi.org/10.1175/JPO-D-15-0087.1

[47]. Savage, A. C., Arbic, B. K., Richman, J. G., Shriver, J. F., Alford, M. H., Buijsman, M. C., et al. (2017). Frequency content of sea surface height variability from internal gravity waves to mesoscale eddies. Journal of Geophysical Research: Oceans, 122(3), 2519-2538. https://doi.org/10.1002/2016JC012331

[48]. Savva, M. A., Kafiabad, H. A., & Vanneste, J. (2021). Inertia-gravity-wave scattering by three-dimensional geostrophic turbulence. Journal of Fluid Mechanics, 916, A6. https://doi.org/10.1017/jfm.2021.205

[49]. Schubert, R., Gula, J., Greatbatch, R. J., Baschek, B., & Biastoch, A. (2020). The submesoscale kinetic energy cascade: Mesoscale absorption of submesoscale mixed layer eddies and frontal downscale fluxes. Journal of Physical Oceanography, 50(9), 2573-2589. https://doi.org/10.1175/JPO-D-19-0311.1

[50]. Shaham, M., & Barkan, R. (2025). Spectral flux decomposition in a wind-driven channel flow with near-inertial waves. Journal of Advances in Modeling Earth Systems, 17(1), e2023MS004036. https://doi.org/10.1029/2023MS004036

[51]. Shakespeare, C. J., & Hogg, A. M. (2017). Spontaneous surface generation and interior amplification of internal waves in a regional-scale ocean model. Journal of Physical Oceanography, 47(4), 811-826. https://doi.org/10.1175/JPO-D-16-0188.1

[52]. Shakespeare, C. J., Gibson, A. H., Hogg, A. M., Bachman, S. D., Keating, S. R., & Velzeboer, N. (2021). A new open source implementation of Lagrangian filtering: A method to identify internal waves in high-resolution simulations. Journal of Advances in Modeling Earth Systems, 13(10), e2021MS002616. https://doi.org/10.1029/2021MS002616

[53]. Shakespeare, C. J., & McC. Hogg, A. (2018). The life cycle of spontaneously generated internal waves. Journal of Physical Oceanography, 48(2), 343-359. https://doi.org/10.1175/JPO-D-17-0153.1

[54]. Skitka, J., Arbic, B. K., Thakur, R., Menemenlis, D., Peltier, W. R., Pan, Y., ... & Ma, Y. (2024). Probing the nonlinear interactions of supertidal internal waves using a high-resolution regional ocean model. Journal of Physical Oceanography, 54(2), 399-425.

Accepted for publication in *Journal of Physical Oceanography*. DOI 10.1175/JPO-D-25-0199.1

https://doi.org/10.1175/JPO-D-22-0236.1

[55]. Srinivasan, K., Barkan, R., & McWilliams, J. C. (2023). A forward energy flux at submesoscales driven by frontogenesis. Journal of Physical Oceanography, 53(1), 287-305. https://doi.org/10.1175/JPO-D-22-0001.1

[56]. Storer, B. A., & Aluie, H. (2023). FlowSieve: A coarse-graining utility for geophysical flows on the sphere. Journal of Open Source Software, 8(84), 4277. https://doi.org/10.21105/joss.04277.

[57]. Storer, B. A., Buzzicotti, M., Khatri, H., Griffies, S. M., & Aluie, H. (2022). Global energy spectrum of the general oceanic circulation. Nature communications, 13(1), 5314. https://doi.org/10.1038/s41467-022-33031-3

[58]. Sugiyama, Y., Niwa, Y., & Hibiya, T. (2009). Numerically reproduced internal wave spectra in the deep ocean. Geophysical research letters, 36(7). https://doi.org/10.1029/2008GL036825

[59]. Taylor, S., & Straub, D. (2020). Effects of adding forced near-inertial motion to a wind-driven channel flow. Journal of Physical Oceanography, 50(10), 2983-2996. https://doi.org/10.1175/JPO-D-19-0299.1

[60]. Thomas, J. (2023). Turbulent wave-balance exchanges in the ocean. Proceedings of the Royal Society A, 479(2276), 20220565. https://doi.org/10.1098/rspa.2022.0565

[61]. Thomas, L. N., Moum, J. N., Qu, L., Hilditch, J. P., Kunze, E., Rainville, L., & Lee, C. M. (2024). BLOCKED DRAINPIPES AND SMOKING CHIMNEYS. Oceanography, 37(4), 22-33. https://doi.org/10.5670/oceanog.2024.304

[62]. Tort, M., & Winters, K. B. (2018). Poleward propagation of near-inertial waves induced by fluctuating winds over a baroclinically unstable zonal jet. Journal of Fluid Mechanics, 834, 510-530. https://doi.org/10.1017/jfm.2017.698

[63]. Weiss, J. (1991). The dynamics of enstrophy transfer in two-dimensional hydrodynamics. Physica D: Nonlinear Phenomena, 48(2-3), 273-294. https://doi.org/10.1016/0167-2789(91)90088-Q

[64]. Whalen, C. B., De Lavergne, C., Naveira Garabato, A. C., Klymak, J. M., MacKinnon, J. A., & Sheen, K. L. (2020). Internal wave-driven mixing: Governing processes and consequences for climate. Nature Reviews Earth & Environment, 1(11), 606-621. https://doi.org/10.1038/s43017-020-0097-z

[65]. Winters, K. B., Lombard, P. N., Riley, J. J., & D'Asaro, E. A. (1995). Available potential energy and mixing in density-stratified fluids. Journal of Fluid Mechanics, 289, 115-128. https://doi.org/10.1017/S002211209500125X

[66]. Wunsch, C., & Ferrari, R. (2018). 100 years of the ocean general circulation. Meteorological Monographs, 59, 7-1.

Accepted for publication in *Journal of Physical Oceanography*. DOI 10.1175/JPO-D-25-0199.1

https://doi.org/10.1175/AMSMONOGRAPHS-D-18-0002.1

[67]. Xu, X., Zhao, W., Huang, X., Hu, Q., Guan, S., Zhou, C., & Tian, J. (2022). Observed near-inertial waves trapped in a propagating anticyclonic eddy. Journal of Physical Oceanography, 52(9), 2029-2047. https://doi.org/10.1175/JPO-D-21-0231.1

[68]. Yang, L., Barkan, R., Srinivasan, K., McWilliams, J. C., Shakespeare, C. J., & Gibson, A. H. (2023). Oceanic eddies induce a rapid formation of an internal wave continuum. Communications Earth & Environment, 4(1), 484. https://doi.org/10.1038/s43247-023-01137-1

[69]. Yu, X., Ponte, A. L., Lahaye, N., Caspar-Cohen, Z., & Menemenlis, D. (2021). Geostrophy assessment and momentum balance of the global oceans in a tide-and eddy-resolving model. Journal of Geophysical Research: Oceans, 126(10), e2021JC017422. https://doi.org/10.1029/2021JC017422

[70]. Zhai, X., Greatbatch, R. J., Eden, C., & Hibiya, T. (2009). On the loss of wind-induced near-inertial energy to turbulent mixing in the upper ocean. Journal of Physical Oceanography, 39(11), 3040-3045. https://doi.org/10.1175/2009JPO4259.1

[71]. Zhang, X., Yu, X., Ponte, A. L., Caspar-Cohen, Z., Le Gentil, S., Wang, L., & Gong, W. (2024). Lagrangian versus Eulerian spectral estimates of surface kinetic energy over the global ocean. Journal of Geophysical Research: Oceans, 129(8), e2024JC021057. https://doi.org/10.1029/2024JC021057

[72]. Zhang, Z., Qiu, B., Tian, J., Zhao, W., & Huang, X. (2018). Latitude-dependent finescale turbulent shear generations in the Pacific tropical-extratropical upper ocean. Nature Communications, 9(1), 4086. https://doi.org/10.1038/s41467-018-06260-8

Accepted for publication in *Journal of Physical Oceanography*. DOI 10.1175/JPO-D-25-0199.1